FINAL TECHNICAL REPORT

NASA GRANT NCC 2-241

PREDICTION AND MEASUREMENT OF HUMAN PILOT DYNAMIC CHARACTERISTICS IN A MANNED ROTORCRAFT SIMULATION

Ronald A. Hess[1] and James T.Reedy[2]

Department of Mechanical Engineering

University of California, Davis

Abstract

An analytical and experimental study of human pilot control strategies in a manned rotorcraft simulation is described. The task simulated involves a low-speed, constant-altitude maneuvering task in which a head-down display is utilized to allow the pilot to track a moving hover point. The efficacy of the display law driving an "acceleration symbol" is determined and the manner in which the prediction and measurement of pilot/vehicle dynamics can be made part of man/machine system evaluations is demonstrated.

[1]Professor, Associate Fellow AIAA

[2]Graduate Student, Student member AIAA

Introduction

Manned simulation continues to be an important research, development and training tool in the aerospace industry. In the area of rotorcraft control/display and handling qualities research, the manned flight simulator allows the safe and efficient evaluation of competing concepts and designs before full-scale vehicle development begins. With escalating simulation costs, it is of utmost importance to extract as much pertinent information regarding the man/machine system as possible from each simulation experiment. It is particularly useful to be able to verify analytical predictions of pilot/vehicle dynamic characteristics in prescribed tasks using simulation data. The work to be described builds upon the work of Ref. 1 and demonstrates how the prediction and measurement of human pilot dynamics can be made part of man/machine system evaluations. The particular task being studied involves a rotorcraft low-speed constant-altitude maneuvering task in which a head-down display is utilized to allow the pilot to track a moving hover point. The "simulator" is unique in that it is the NASA-Ames CH-47B variable stability rotorcraft used in a fixed-base simulation mode. The specfic goal of the research to be described is the analytical and experimental evaluation of a particular display control law aimed at reducing pilot workload and increasing pilot performance in hovering flight.

Vehicle and Task

The research of this study has an antecendent in the flight experiments reported in Reference 2. That study involved a preliminary flight test evaluation of the effects of control/display compatibility upon hovering rotorcraft handling qualities. The tests utilized the aforementioned CH-47B

rotorcraft in flight rather than in simulation mode. Flight tasks consisted of so-called "pad captures" and "pad tracking" in low-speed, near-hover conditions. The primary cockpit display for the evaluation pilots was a color, panel-mounted display shown in Fig. 1, with symbology defined. The display was based upon the current Pilot Night Vision System head-up display in the Army AH-64 Apache attack helicopter [3].

Three control-response systems were utilized in Ref. 2: an angular rate-command/attitude hold system (RATE), an attitude command/attitude hold system (ATTITUDE), and a velocity command/attitude hold system (VELOCITY). In the display shown in Fig. 1, the "acceleration symbol" was driven by a display law which allowed it to be treated like a flight director by the pilot. That is, by moving the cyclic control so that the symbol moved to and remained centered on the hover position symbol, the rotorcraft flew to and remained over the hover pad. In the "pad capture" task, the displayed pad symbol would undergo a single discrete position change on the display. The pilot was to fly the vehicle to the displaced pad and stabilize in a hover. In the "pad tracking" task, the displayed pad symbol was driven by sums of sinusoids in the longitudinal and lateral direction. Here the pilot was to attempt to keep the vehicle over the pad symbol at all times. The tasks were conducted "head down" so that the use out-the-window visual cues was minimized.

The philosophy behind the design of the acceleration symbol and its display law is explained in Ref. 2. The goal was to relieve the pilot of the workload associated with the instrument scanning and information integration which normally accompanies hovering flight under Instrument Meteorological

Conditions. Thus, the piloting task was simplified to the control a single display element in the pad capture and tracking tasks. Ideally, the dynamics of the vehicle/display system would be such that the pilot could control the vehicle with very little compensation. In general, the results of Ref. 2 indicated that the acceleration ball was a useful display concept, with potential for improving mission performance and reducing pilot workload.

As mentioned in the Introduction, the specific objective of the research reported herein is the analytical and experimental evaluation of the acceleration symbol display law used in the head-down display of Ref. 2. A secondary objective was the demonstration of how the prediction and measurement of pilot/vehicle dynamics can be made part of man/machine system evaluations. Only the ATTITUDE system and the pad tracking task was chosen for analysis and experimental evaluation in this study.

Simulation

As stated in the Introduction, the CH-47B variable stability rotorcraft was used in this study in a fixed-base simulator mode. The display, cockpit controls, etc., were the same as use in the flight tests of Ref. 2. The tracking runs were approximately two minutes in length, with 102.4 secs of data used in the analysis. Two test subjects were utilized in the simulation, one a test pilot, the second an engineer. In addition to informal training runs, each subject completed five data runs on each of the configurations studied. The ATTITUDE response system was always employed and the configurations differed in the number of axes being controlled (longitudinal and lateral, or just longitudinal) and in the display content (display with and without

acceleration symbol). Table 1 gives the pertinent data on vehicle dynamics.

The techniques used to measure pilot/vehicle dynamics in this study were the Fast Fourier Transform (FFT) and the least squares error (LSE) techniques discussed in Ref. 1. In the simulation, as in the flight test, the hover pad symbol was driven in the longitudinal and lateral directions by two sums of sinusoids with different constituent frequencies. Sums of sinusoids were chosen as pad driving functions as opposed to purely random inputs so that the power and cross power spectral densities used in measuring pertinent pilot/vehicle transfer functions could be replaced by products of Fourier coefficients, themselves obtained via the FFT technique. With a .05 sec sampling interval in the simulation, the data length of 102.4 secs provided the required "power of 2" number of data points for use in the FFT analysis [4]. The sums of sinusoids are shown in Table 2. The frequencies and amplitudes were chosen to provide adequate power at frequencies of interest for manual control while still presenting a realistic, albeit demanding, task to the pilot.

Figures 2 and 3 show the pilot/vehicle system to be discussed in more detail in the following section. Figure 2 indicates the hypothesized pilot loop closures in the pad tracking task when no acceleration symbol is provided, while Fig. 3 shows the hypothesized pilot loop closures when the acceleration symbol is provided. Referring to these figures, three different transfer functions were measured in the simulation: x/x_{pad}, x_{ball}/x_{pad} and $x_{ball}/(x_a - x_{ball})$ "x_{pad}" refers to the pad postion relative to a reference point on the earth in a direction parallel to the instantaneous x body axis of

the vehicle, while "x" refers to the vehicle position relative to the same point in the same direction. "x_e" refers to the relative longitudinal positions of the pad and the vehicle. It is only this latter quantity which is displayed to the pilot in Fig. 1 as the vertical distance between the center of the display and the pad symbol. "x_{ball}" refers to the longitudinal acceleration symbol position, again relative to the center of the display. The x/x_{pad} transfer funtion was particularly useful since it correlated strongly with pad tracking performance and could be defined and measured with and without the acceleration symbol present.

Figures 4-17 show the experimental results. The solid dark lines represent all the results of the LSE measurments interpreted in the w' plane [1] and the cirlces and vertical bars indicate the means and standard deviations of the FFT measurements at the input frequencies of Table 1. Given the sampling frequency of .05 secs and the frequency range of interest for manual control ($\omega <$ 20 rad/sec), the w' and s planes can be considered equivalent. All the LSE measurements were based upon the following z-transfer function model:

$$H(z) = \{[b_1 z^{-1}+b_2 z^{-2}+b_3 z^{-3}]/[1-a_1 z^{-1}-a_2 z^{-2}-a_3 z^{-3}]\}z^{-p} \qquad (1)$$

This model was selected because it was felt to possess enough degrees of freedom to adequtely identify all the pilot/vehicle transfer functions of interest in this study. In addition to the six a_i and b_i parameters, the LSE program also identified any constant biases in the data serving as the model input. The delay parameter p was not included in the least-squares

identification, itself. Rather p was incremented from zero in a series of identification runs for each system to be identified and the set of model parameters yielding the best model fit was selected. The quality of the LSE transfer function fits was ascertained using the correlation coefficient defined as

$$R^2 = 1.0 - [\sum (y_k - y_k')^2]/[\sum (y_k)^2] \qquad (2)$$

where y_k and y_k' are, respectively, the measured output and identified model output [1]. The mean R^2 values are indicated on each of the figures. It should be noted that the LSE method yielded either unstable transfer functions (R^2 unbounded) or very low R^2 values for the pilot/vehicle transfer function $x_{ball}/(x_e - x_{ball})$. An explanation for this will be offered in the Discussion.

Pilot/Vehicle Analysis

Referring back to Fig. 2, one sees that without the acceleration symbol, three loops need to be closed by the pilot, with the inner most loop referred to herein as the "primary control loop", i.e. that loop involving human interaction with a control manipulator. It is the necessity of closing the outer loops which leads to the pilot workload associated with display scanning and control. Comparing Figs. 2 and 3, one sees the simplification afforded by the acceleration symbol. As opposed to the three loops which have to be closed by the pilot in Fig. 2, only two are closed in Fig. 3. Obviously identical pilot control strategies and completely analogous variables can be defined for the lateral vehicle control problem, but these will not be discussed here.

Figure 18 is a Bode plot of the transfer function between acceleration symbol movement on the display and control input for the longitudinal ATTITUDE response system. This transfer function represents the effective "controlled element" in the primary control loop when the acceleration symbol is being used. The lateral system is very similar, but again, will not be discussed here. As can be seen, the transfer function begins to resemble a pure gain for frequencies above around 1 rad/sec. According to the "crossover model" of the human pilot [5], the pilot will have to develop lag compensation (element G_1 in Fig. 3) in the primary control loop over this frequency range in order for the product of pilot and controlled element transfer functions to resemble K/s for frequencies above 1 rad/sec.

Figure 19 shows a diagram of the structural model of the human pilot which will be used to model pilot dynamics in the primary control loop in this study. This model has been discussed in the literature and the reader is referred to Refs. 6 and 7 for details. Nominal values for the model parameters can be chosen via a technique outlined in Ref. 6. These paramters are given in Table 3 for the case of lag compensation. Figure 20 shows the Bode plot of the predicted pilot transfer G_1. Figure 21 shows the product of this transfer function and that of the "controlled element", whose Bode plot is shown in Fig. 18. In Fig. 21, the value of the pilot gain K_c has been changed from the nominal value of unity to 1.57 to give a crossover frequency of 2.0 rad/sec. This value was used an an initial estimate for the task.

Figure 22 shows the effective "controlled element" for the outer loop closure in Fig. 3. As discussed in Ref. 6, pilot dynamics in multi-loop tasks

such as Fig. 3 can be obtained by multiple applications of the crossover model, with a separation between crossover frequencies of a factor of approximately 4 for successive closures. Since the outer-loop in Fig. 3 is not a primary control loop, the structural model is not employed. Rather the required pilot compensaton is generated by simple proportional-integral-derivative (PID) dynamics. Figure 22 indicates that a $G_2 = 1.0$ would yield a crossover frequency of 0.2 rad/sec and K/s-like dynamics around crossover. However, the measured x_{ball}/x_{pad} transfer functions of Figs. 10-13 clearly indicate that a pure gain outer closure is not occuring. The transfer function x_{ball}/x_{pad} can be considered as a product of two other transfer functions as

$$x_{ball}/x_{pad} = [x_{ball}/x_e][x_e/x_{pad}] \quad (3)$$

Now the second of these, x_e/x_{pad}, is the error-to-input transfer function for the outer loop in the pad tracking task. Defining closed-loop bandwidth as the frequency where the phase of x/x_{pad} goes through -90°, Figs. 4-7 indicate a bandwidth of approximately 0.6 rad/sec. This means that the x_e/x_{pad} transfer functions will be very close to unity for all frequencies beyond around 1.0 rad/sec. Thus, Eq. 3 indicates that for $\omega > 1.0$ rad/sec,

$$x_{ball}/x_{pad} \approx x_{ball}/x_e \quad (4)$$

Equation 4 now presents an inconsistency in the modeling formulation if $G_2 = 1.0$. The data of Figs. 10-13 clearly indicate that above 1.0 rad/sec, $|x_{ball}/x_{pad}|$ (and hence $|x_{ball}/x_e|$) are approximately equal to unity. However, with $G_2 = 1.0$

$$x_{ball}/x_e = G_1(x_{ball}/\delta)/[1 + G_1(x_{ball}/\delta)] \quad (5)$$

and the amplitude of this transfer function rolls off rapidly after 2.0 rad/sec. However, if $G_2 = (Ts + 1)$, then

$$x_{ball}/x_e = (Ts + 1)[G_1(x_{ball}/\delta)/(1 + G_1(x_{ball}/\delta)] \quad (6)$$

Selecting $T \approx 0.5$ sec, will result in the amplitude of the transfer function of Eq. 6 remaining close to unity above 2.0 rad/sec, as indicated by the measurments of Figs. 10-13. With $G_2 = (0.5s + 1)$, the transfer functions x/x_{pad} and x_{ball}/x_{pad} obtained with the pilot model G_1 and G_2 closely resemble those obtained in experiment.

Now with a non-unity G_2, the measured transfer function $x_{ball}/(x_e-x_{ball})$ becomes a "composite" of the pilot dynamics G_1 and G_2:

$$x_{ball}/(x_e-x_{ball}) = G_1(x_{ball}/\delta)G_2/[1 + G_1(x_{ball}/\delta)(1-G_2)] \quad (7)$$

Figure 23 shows the Bode plot associated with the transfer function of Eq. 7 plotted on the experimental $x_{ball}/(x_e-x_{ball})$ data of Fig. 14. Here, the value of K_e in Table 3 was changed from the nominal value of unity to 0.78. In addition, a delay of 0.1 sec was added to G_2 yielding

$$G_2 = (0.5s + 1)\exp(-0.1s). \quad (8)$$

This delay can be attributed to the lead compensation required in the outer-

loop. It should be noted that the addition of the delay to G_2 made only very minor changes to the transfer functions x/x_{pad} and x_{ball}/x_{pad} discussed in the previous paragraph. The comparison in Fig. 23 is felt to be acceptable for the purposes of this study. With the change in K_e just noted, the open-loop pilot/vehicle transfer function G_1(xball/δ) for the inner-loop of Fig. 3 now exhibits a crossover frequency of 1.0 rad/sec. This means that the crossover frequency separation between the inner and outer loops of Fig. 3 is 5, which compares favorably with the rule-of-thumb factor of 4 quoted previously.

Discussion

When compared to Figs. 4-7, Figs. 8 and 9 indicate that when the acceleration symbol is removed from the display, the closed-loop transfer function x/x_{pad} exhibits much lower values of closed-loop damping and a considerably larger spread in the FFT and LSE measurements as well as the mean R^2 values than when the symbol is present. This is convincing evidence supporting the effectiveness of the acceleration symbol and the display law used to drive it. The utility of the symbol is also reflected in the average root-mean-square (RMS) position error between vehicle and pad, where it was found that an average 44% increase in RMS error accompanied a removal of the acceleration symbol.

Figure 24 shows a comparison of helicopter longitudinal motion time histories for one of the runs. The trace labeled "actual" represents the actual the helicopter longitudinal position x. The trace labeled "command" represents the variable x_{pad}, the command position. Finally, the trace labeled "simulation" represents the variable x that results when the pilot/vehicle

dynamics are replaced with the LSE identified x/x_{pad} transfer function and the x_{pad} command applied. Thus, the difference between the "actual" and "simulated" traces gives an indication of the quality of the identification. The relatively large errors between the "command" and "actual" traces in Fig. 24a,b is an indication of the challenging nature of the pad tracking task.

The phenomena of the LSE identification converging to unstable transfer functions or producing unacceptably low R^2 values for $x_{ball}/(x_c-x_{ball})$ can be explained by the fact that $x_{ball}/(x_c-x_{ball})$ is actually a <u>composite</u> transfer function and, as such, can exhibit dynamics which are difficult to identify via LSE techniques. For example, some of the FFT data of Figs. 14-17 clearly indicate low frequency phase lags (often called "phase droop") which could lead to an unstable pole in the LSE identified transfer function. It should be noted that changing the order of the H(z) model in Eq. 1 did not solve the problem. Of course, the FFT identification approach is immune to these problems since it does not attempt to generate a transfer function, <u>per se</u>, but only transfer function amplitude and phase information at the discrete input frequencies.

A comparison of the closed-loop transfer function x/x_{pad} using the pilot model transfer functions G_1 and G_2 was undertaken for two cases: (1) with G_2 = (.5s + 1)exp(-0.1s) and using G_1 with K_c = 0.78, and (2) with G_2 = 1.0 and using G_1 with K_c = 1.0. Recall that the smaller K_c value lowered the crossover frequency of the inner loop of Fig. 3 from the initial estimate of 2.0 rad/sec to 1.0 rad/sec. This comparison indicated nearly identical x/x_{pad} transfer functions, implying very comparable pad tracking performance. Thus, the outer

crossover frequency while not suffering a performance penalty. Although it is speculative at this point, it is not unreasonable to assume that the pilot workload decrement associated with the lower inner-loop crossover frequency more than compensates for the workload increment associated with lead equalization in the outer-loop. The small workload penalty for lead equalization in the outer-loop is probably attributable to the nature of the display symbology, itself.

Summary

A pilot/vehicle analysis using structural an crossover models of the human pilot has provided an analytical framework within which to interpret the results of a manned rotorcraft simulation. Simulation data was analyzed using both frequency and time domain measures to obtain pilot/vehicle transfer functions. The efficacy of a particular display symbology was demonstrated in an objective manner, i.e., without reliance upon pilot opinion ratings. The methodology discussed herein can and should be made part of any manned simulation in which well-defined tasks are undertaken by the human.

Acknowledgement

This work was performed under grant No. NCC2-241, NASA Ames Research Center, Dryden Flight Research Facility. Mr. Donald T. Berry was the contract monitor. The authors are indebted to Mr. Edwin Aiken and Ms. Michelle Eshow of the Flight Dynamics and Controls Branch at NASA Ames Research Center for their help in the simulation experiment which made this study possible.

References

[1] Hess, R. A., and Mnich, M. A., "Identification of Pilot-Vehicle Dynamics Using In-Flight Tracking Data," Journal of Guidance, Control and Dynamics, Vol. 9, No. 4, July-August, 1986, pp. 433-440.

[2] Eschow, M. M., Aiken E. W., and Hindson, W. S., "Preliminary Results of a Flight Investigation of Rotorcraft Control and Display Laws for Hover," American Helicopter Society Mideast Region National Specialists' Meeting in Rotorcraft Flight Controls and Avionics, Oct. 13-15, 1987, Cherry-Hill, New Jersey.

[3] Tsoubanos, C. M., and Kelley, M. B., "Pilot Night Vision System (PNVS) for Advanced Attack Helicopter (AAH)," American Helicopter Society 84th Annual National Forum, Washington, DC.

[4] Bendat, J. S., and Piersol A. G., Random data: Analysis and Measurment Procedures, John Wiley and Sons, 1971.

[5] McRuer, D. T., and Krendel, E. S., "Mathematical Models of Human Pilot Behavior," AGARDograph No. 188, Jan. 1974.

[6] Hess, R. A., "Investigating Aircraft Handling Qualities Using a Structural Model of the Human Pilot," AIAA Paper No. 87-2537, AIAA Guidance, Navigation and Control Conference, Montery, California, August 17-19, 1987.

[7] Hess, R. A., "A Model-Based Theory for Analyzing Human Control Behavior," in Advances in Man-Machine Systems Research, Vol. 2, W. B. Rouse, Ed., JAI Press, pp. 129-176.

Figure Captions

Figure 1. The display symbology.

Figure 2. Hypothesized pilot loop closures without acceleration symbol.

Figure 3. Hypothesized pilot loop closures with acceleration symbol.

Figure 4. x/x_{pad} transfer function for subject 1, longitudinal tracking only, with acceleration symbol.

Figure 5. x/x_{pad} transfer function for subject 2, longitudinal tracking only, with acceleration symbol.

Figure 6. x/x_{pad} transfer function for subject 1, longitudinal and lateral tracking, with acceleration symbol.

Figure 7. x/x_{pad} transfer function for subject 2, longitudinal and lateral tracking, with acceleration symbol.

Figure 8. x/x_{pad} transfer function for subject 1, longitudinal and lateral tracking, without acceleration symbol.

Figure 9. x/x_{pad} transfer function for subject 2, longitudinal and lateral tracking, without acceleration symbol.

Figure 10. x_{ball}/x_{pad} transfer function for subject 1, longitudinal tracking only, with acceleration symbol.

Figure 11. x_{ball}/x_{pad} transfer function for subject 2, longitudinal tracking only, with acceleration symbol.

Figure 12. x_{ball}/x_{pad} transfer function for subject 1, longitudinal and lateral tracking, with acceleration symbol.

Figure 13. x_{ball}/x_{pad} transfer function for subject 2, longitudinal and lateral tracking, with acceleration symbol.

Figure 14. $x_{ball}/(x_c-x_{ball})$ transfer function for subject 1, longitudinal tracking only, with acceleration symbol.

Figure 15. $x_{ball}/(x_c-x_{ball})$ transfer function for subject 2, longitudinal tracking only, with acceleration symbol.

Figure 16. $x_{ball}/(x_c-x_{ball})$ transfer function for subject 1, longitudinal and lateral tracking, with acceleration symbol.

Figure 17. $x_{ball}/(x_c-x_{ball})$ transfer function for subject 2, longitudinal and lateral tracking, with acceleration symbol.

Figure 18. x_{ball}/δ transfer function for ATTITUDE flight control system.

Figure 19. The structural model of the human pilot.

Figure 20. Predicted pilot transfer function G_1 using structural model of Fig. 19.

Figure 21. $G_1(x_{ball}/\delta)$ transfer function.

Figure 22. $x/x_{ball\ comm}$ transfer function.

Figure 23. Comparison of model-based $x_{ball}/(x_c-x_{ball})$ transfer function with data from Fig. 14.

Figure 24. Comparison commanded, actual and simulated helicopter longitudinal position time histories for subject 1, longitudinal and lateral tracking, (a) with acceleration symbol, (b) without acceleration symbol.

Table 1. Rotorcraft Longitudinal Control and Display Dynamics

Attitude Command/Attitude Hold System Dynamics

$$\theta/\delta = 0.28/[s^2 + 2s + 2] \quad \text{rad/in}$$

Translational Dynamics

$$x/\theta = -32.2/[s(s + .04)] \quad \text{ft/rad}$$

Acceleration Symbol Dynamics

$$x_{bmll}/\delta =$$

$$3.6[(s^2 + 1.96s + 1.94)(s^2 + 2.08s + 2.065)]/[(s + 1)(s + .04)(s^2 + 2s + 2)$$

"screen units"/in

Table 2. Sums of Sinusoids for Pad Tracking Task

$$x_{pad} = 4.4\{\sin(.1841t) + \sin(.3068t) + \sin(.4909t) + \sin(.7977t) + 0.1[\sin(1.166t) + \sin(1.779t) + \sin(2.823t)] + 0.05[\sin(4.663t) + \sin(6.934t)]\} \text{ ft}$$

$$y_{pad} = 4.4\{\sin(.2454t) + \sin(.4295t) + \sin(.6750t) + \sin(.9204t) + 0.1[\sin(1.411t) + \sin(2.270t) + \sin(3.743t)] + 0.05[\sin(5.706t) + \sin(7.793t)]\} \text{ ft}$$

Table 3. Pilot Model Paramaters

K_e	= 1.54	T_1	= 5.0 secs
τ_o	= 0.14 secs	K_2	= 2.0
ω_n	= 10.0 rad/sec	T_2	= 1.0 secs
ζ_n	= 0.707	k	= 0
K_1	= 1.0	K_v	= 0 (no motion)

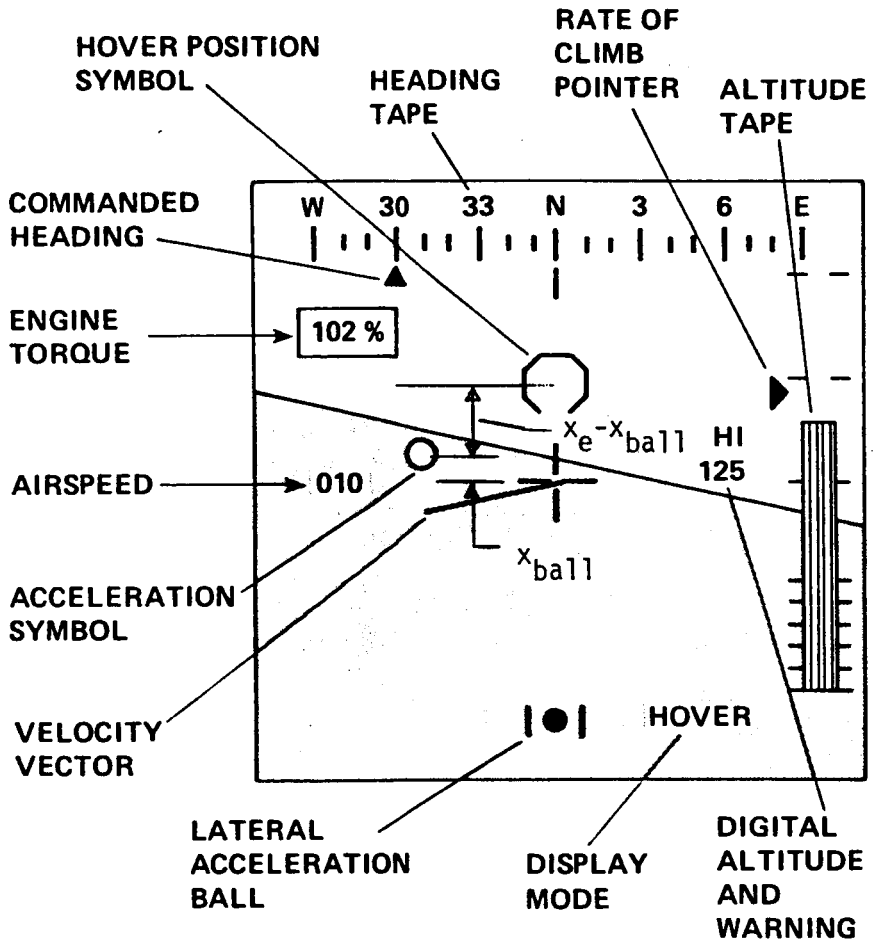
HOVER POSITION SYMBOL
HEADING TAPE
RATE OF CLIMB POINTER
ALTITUDE TAPE
COMMANDED HEADING
W 30 33 N 3 6 E
ENGINE TORQUE
102 %
$x_e - x_{ball}$
HI
125
AIRSPEED
010
x_{ball}
ACCELERATION SYMBOL
VELOCITY VECTOR
HOVER
LATERAL ACCELERATION BALL
DISPLAY MODE
DIGITAL ALTITUDE AND WARNING

Fig. 1

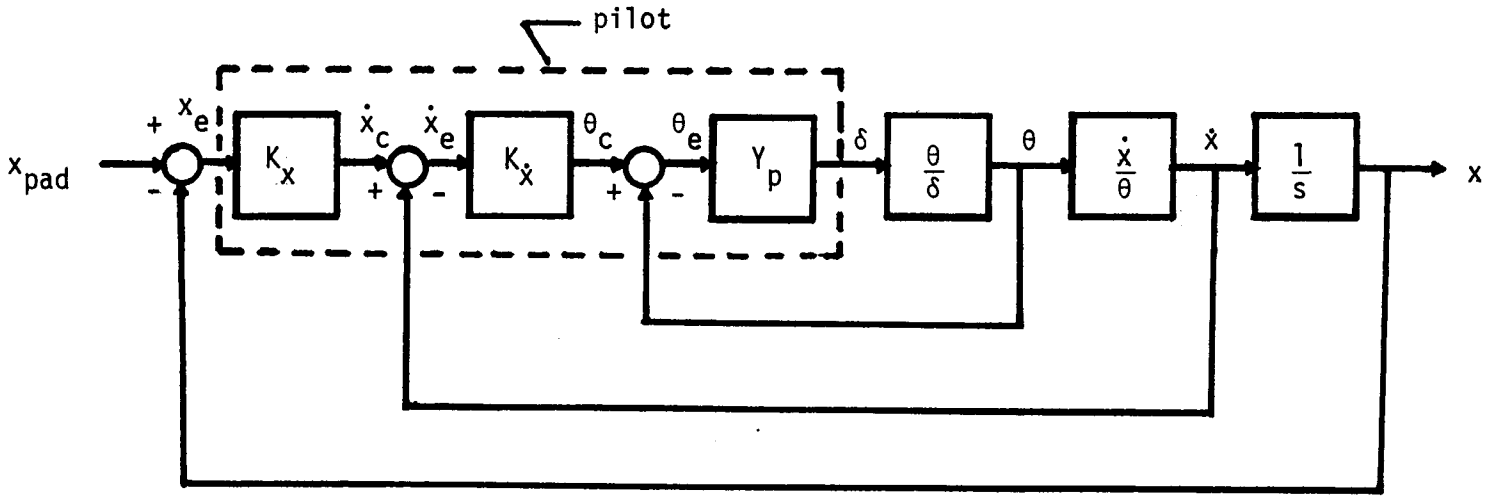
pilot
x_{pad}
+
-
x_e
K_x
$\dot{x}_c$
+
-
$\dot{x}_e$
$K_{\dot{x}}$
θ_c
+
-
θ_e
Y_p
δ
$\frac{\theta}{\delta}$
θ
$\frac{\dot{x}}{\theta}$
$\dot{x}$
$\frac{1}{s}$
x

Fig. 2

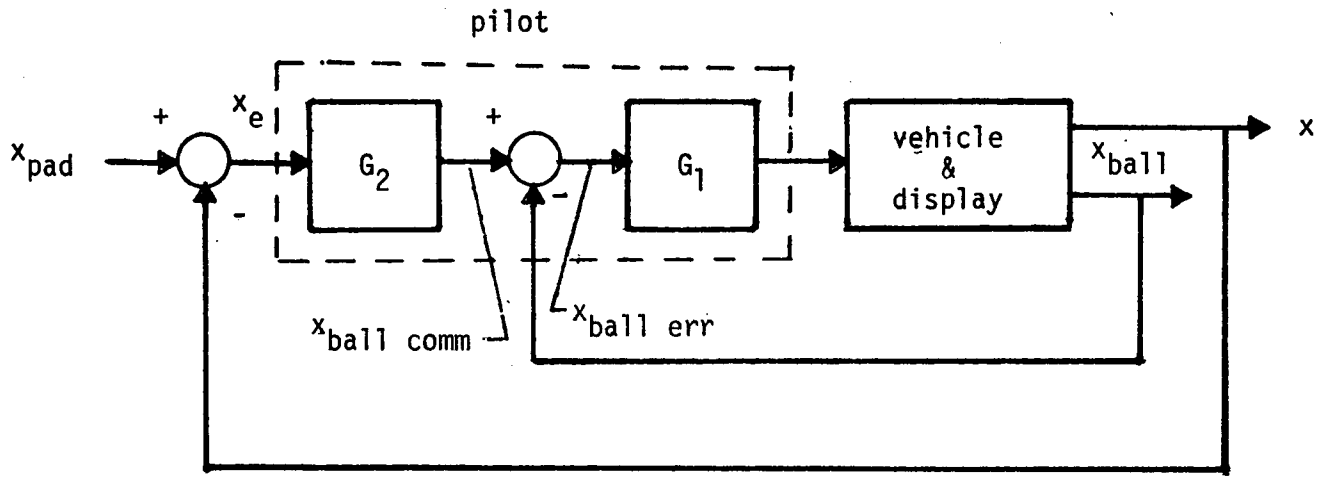
pilot
+
x_e
+
x_{pad}
-
G_2
-
G_1
vehicle
&
display
x_{ball}
x
$x_{ball\ comm}$
$x_{ball\ err}$

Fig. 3

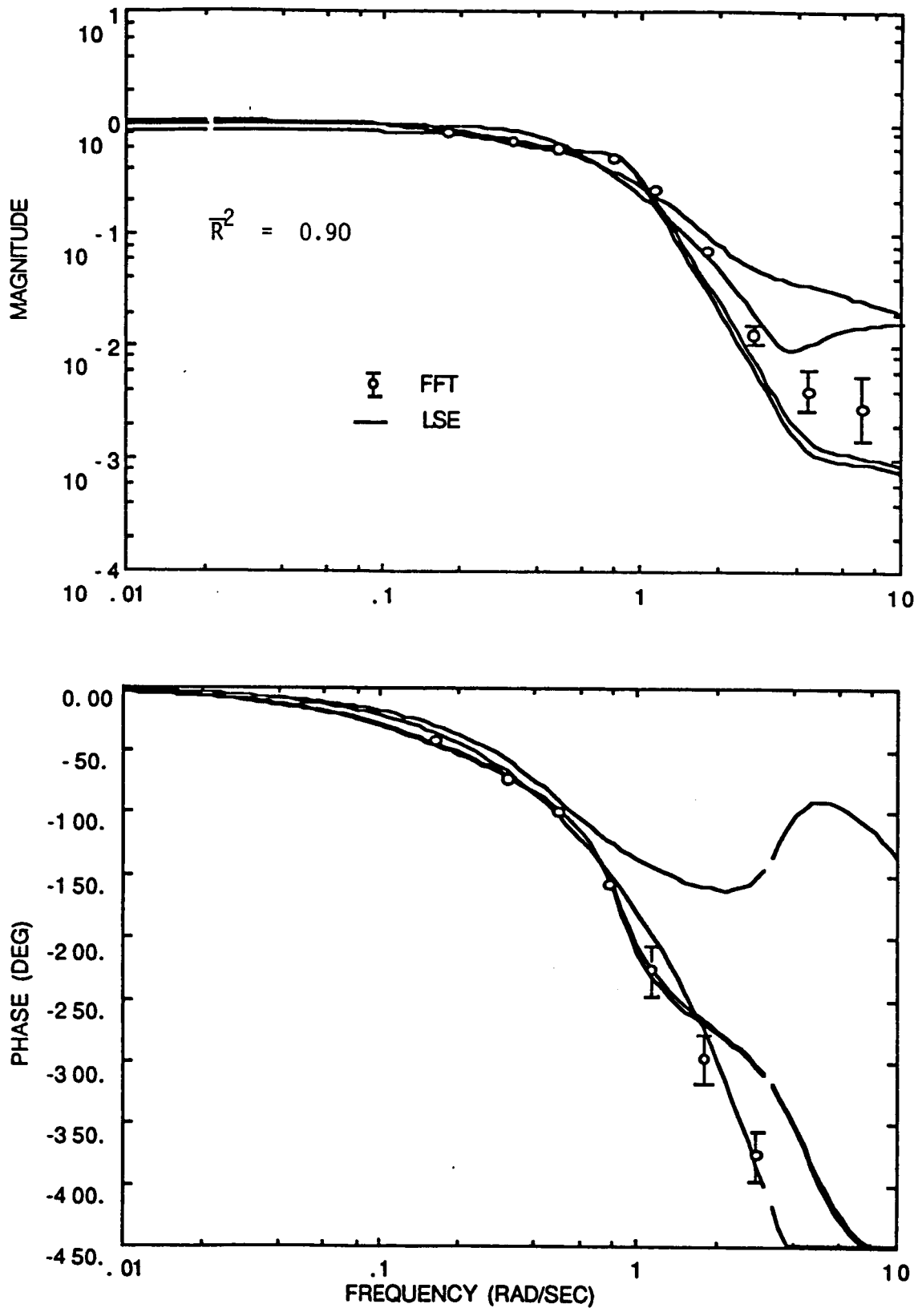
MAGNITUDE
10^{1}
10^{0}
10^{-1}
10^{-2}
10^{-3}
10^{-4}
R^2 = 0.90
FFT
LSE
.01
.1
1
10
PHASE (DEG)
0.00
-50.
-100.
-150.
-200.
-250.
-300.
-350.
-400.
-450.
FREQUENCY (RAD/SEC)

Fig. 4

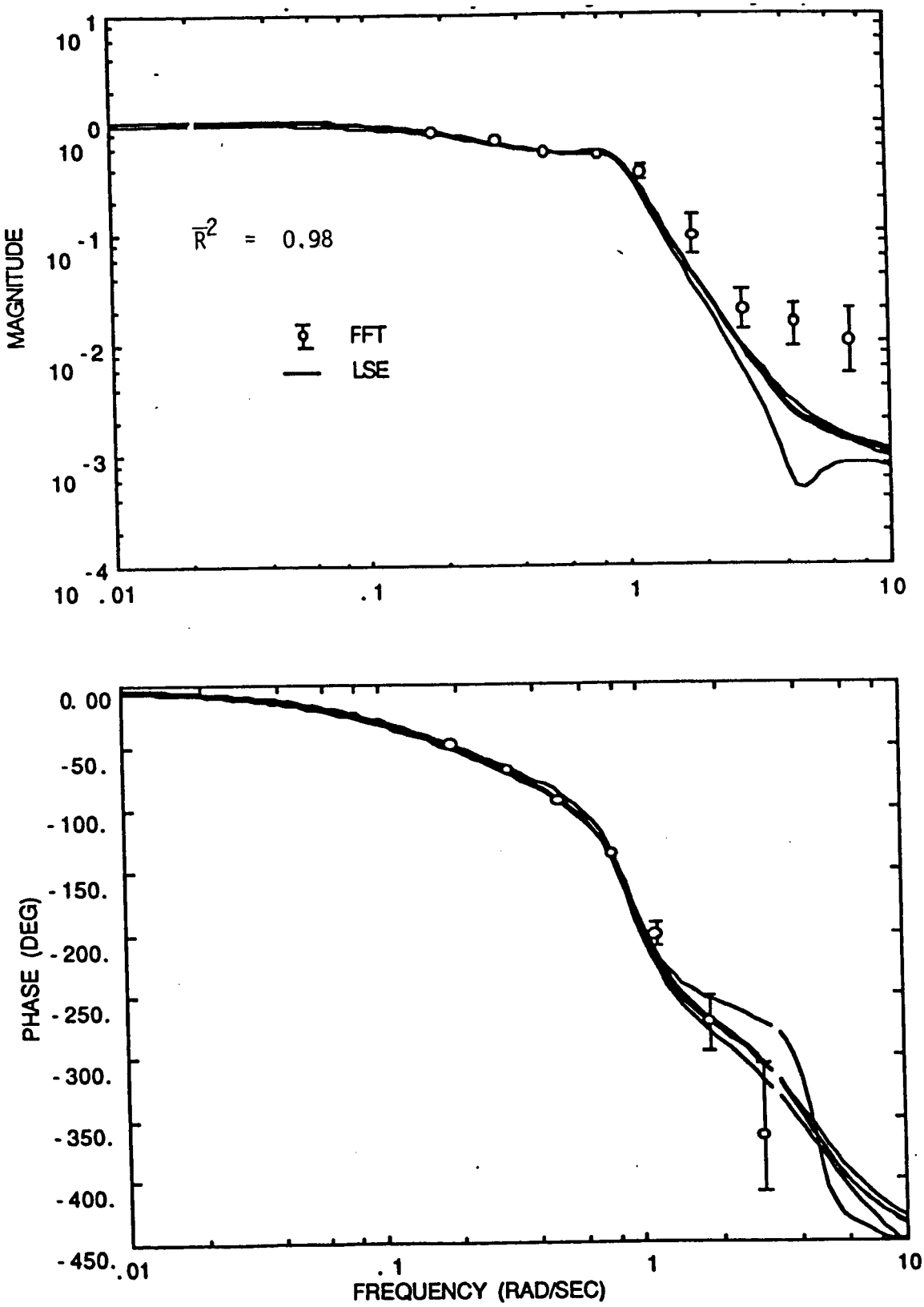
MAGNITUDE
10^{1}
10^{0}
10^{-1}
10^{-2}
10^{-3}
10^{-4}
$\bar{R}^2$ = 0.98
FFT
LSE
.01
.1
1
10
PHASE (DEG)
0.00
-50.
-100.
-150.
-200.
-250.
-300.
-350.
-400.
-450.
FREQUENCY (RAD/SEC)

Fig. 5

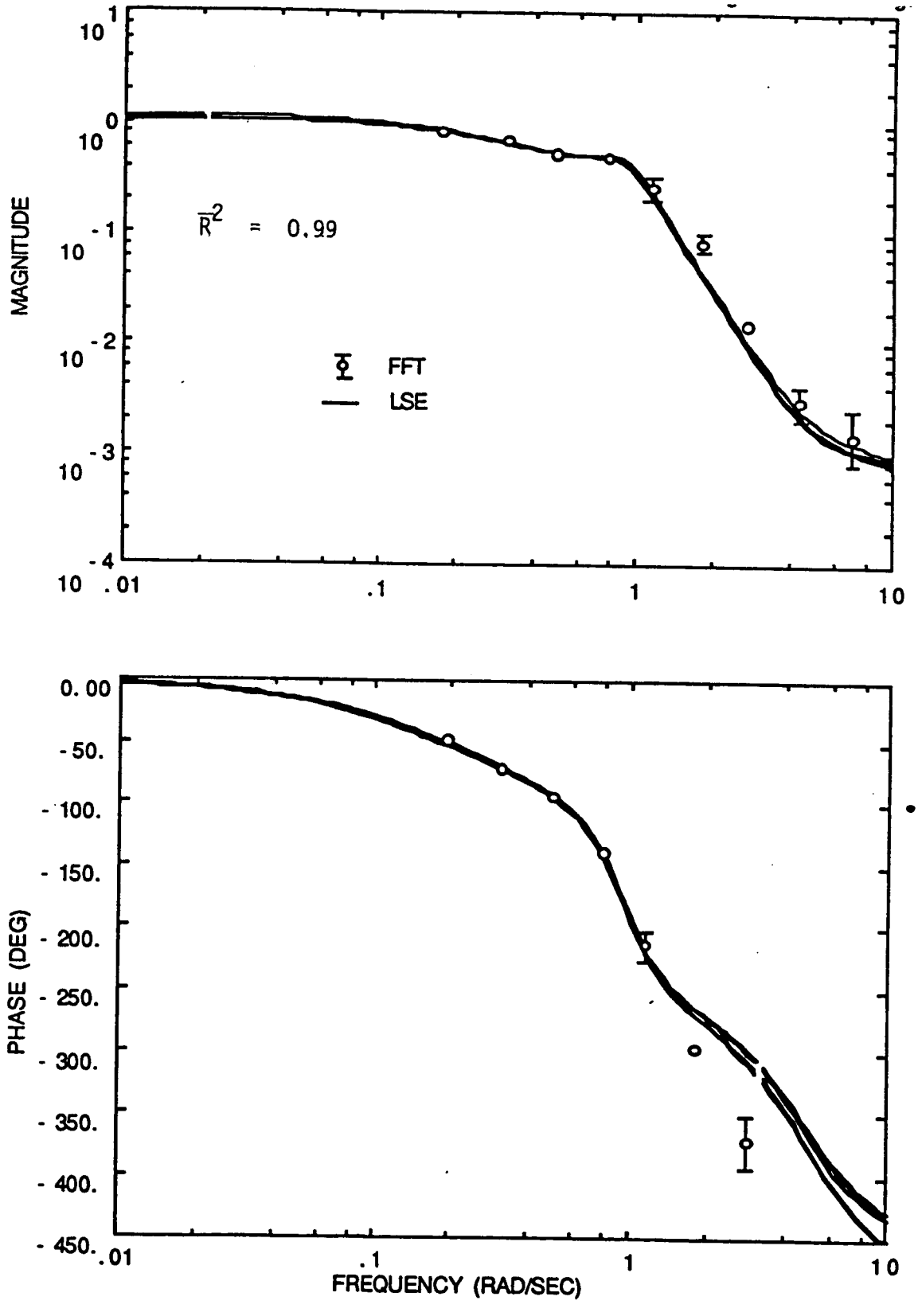
MAGNITUDE
10^{1}
10^{0}
10^{-1}
10^{-2}
10^{-3}
10^{-4}
$\bar{R}^2$ = 0.99
FFT
LSE
.01
.1
1
10
PHASE (DEG)
0.00
-50.
-100.
-150.
-200.
-250.
-300.
-350.
-400.
-450.
FREQUENCY (RAD/SEC)

Fig. 6

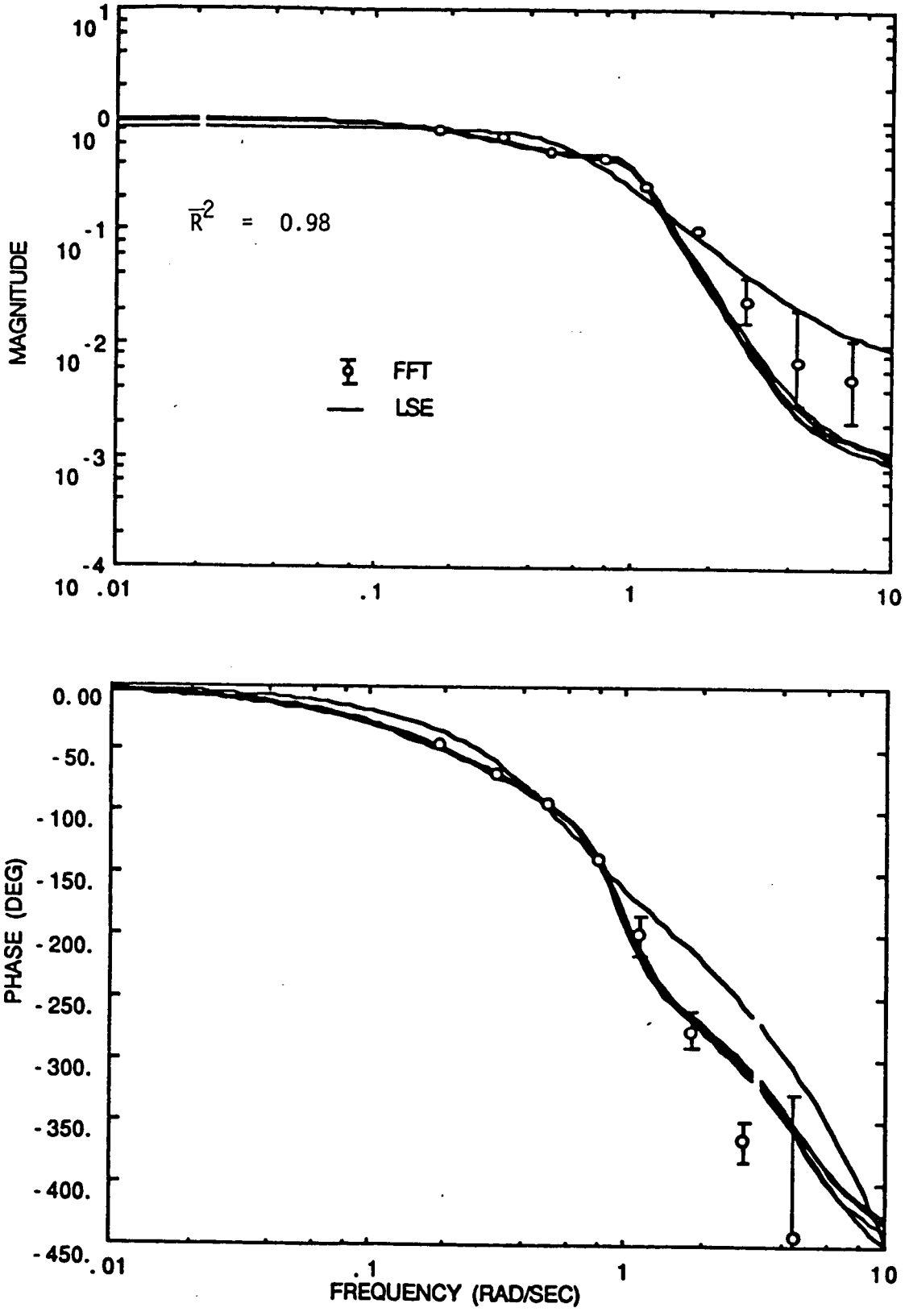
MAGNITUDE
10^{1}
10^{0}
10^{-1}
10^{-2}
10^{-3}
10^{-4}
$\overline{R}^2$ = 0.98
FFT
LSE
.01
.1
1
10
PHASE (DEG)
0.00
-50.
-100.
-150.
-200.
-250.
-300.
-350.
-400.
-450.
FREQUENCY (RAD/SEC)

Fig. 7

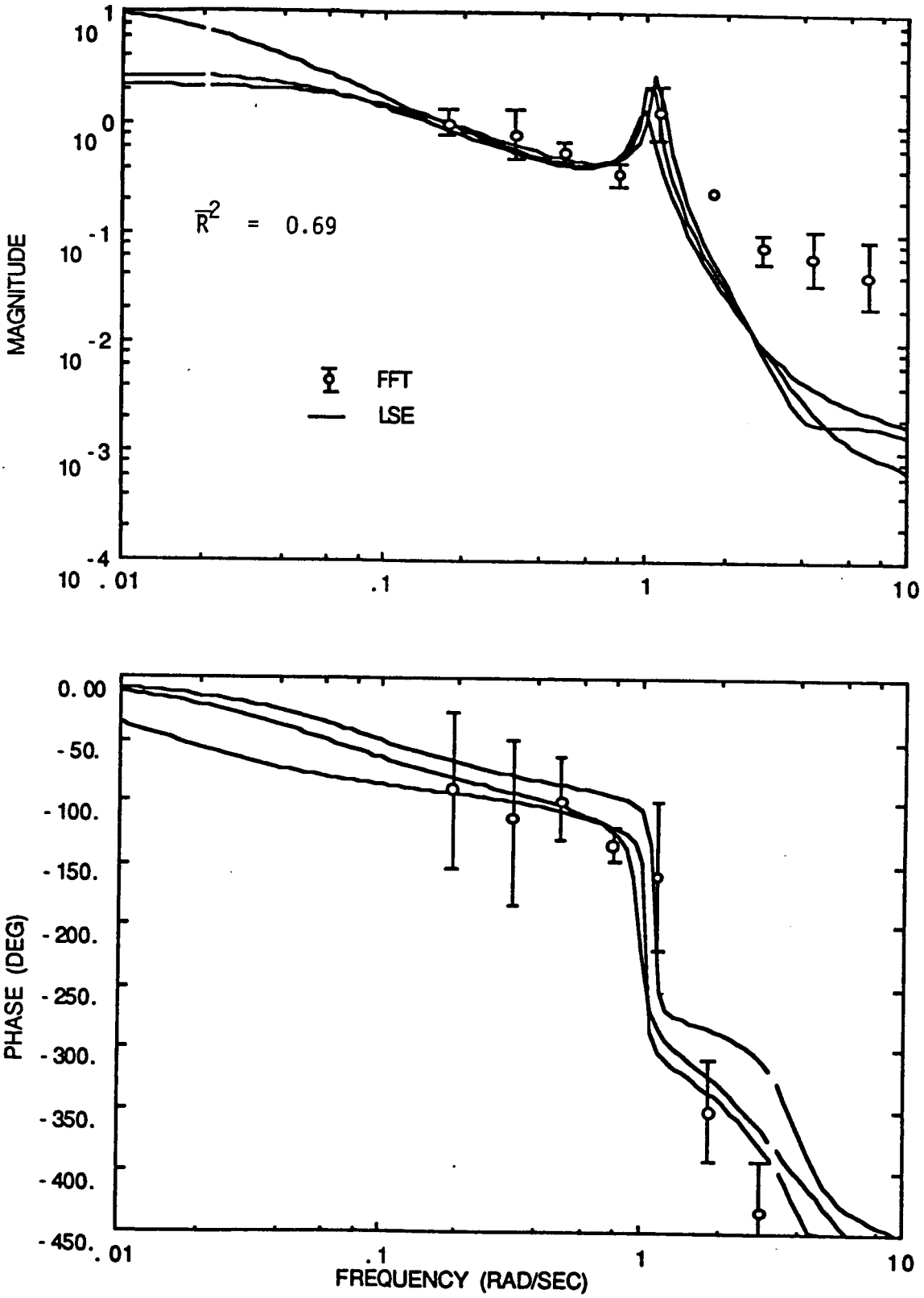
MAGNITUDE
10^{1}
10^{0}
10^{-1}
10^{-2}
10^{-3}
10^{-4}
$\bar{R}^2$ = 0.69
FFT
LSE
.01
.1
1
10
PHASE (DEG)
0.00
-50.
-100.
-150.
-200.
-250.
-300.
-350.
-400.
-450.
FREQUENCY (RAD/SEC)

Fig. 8

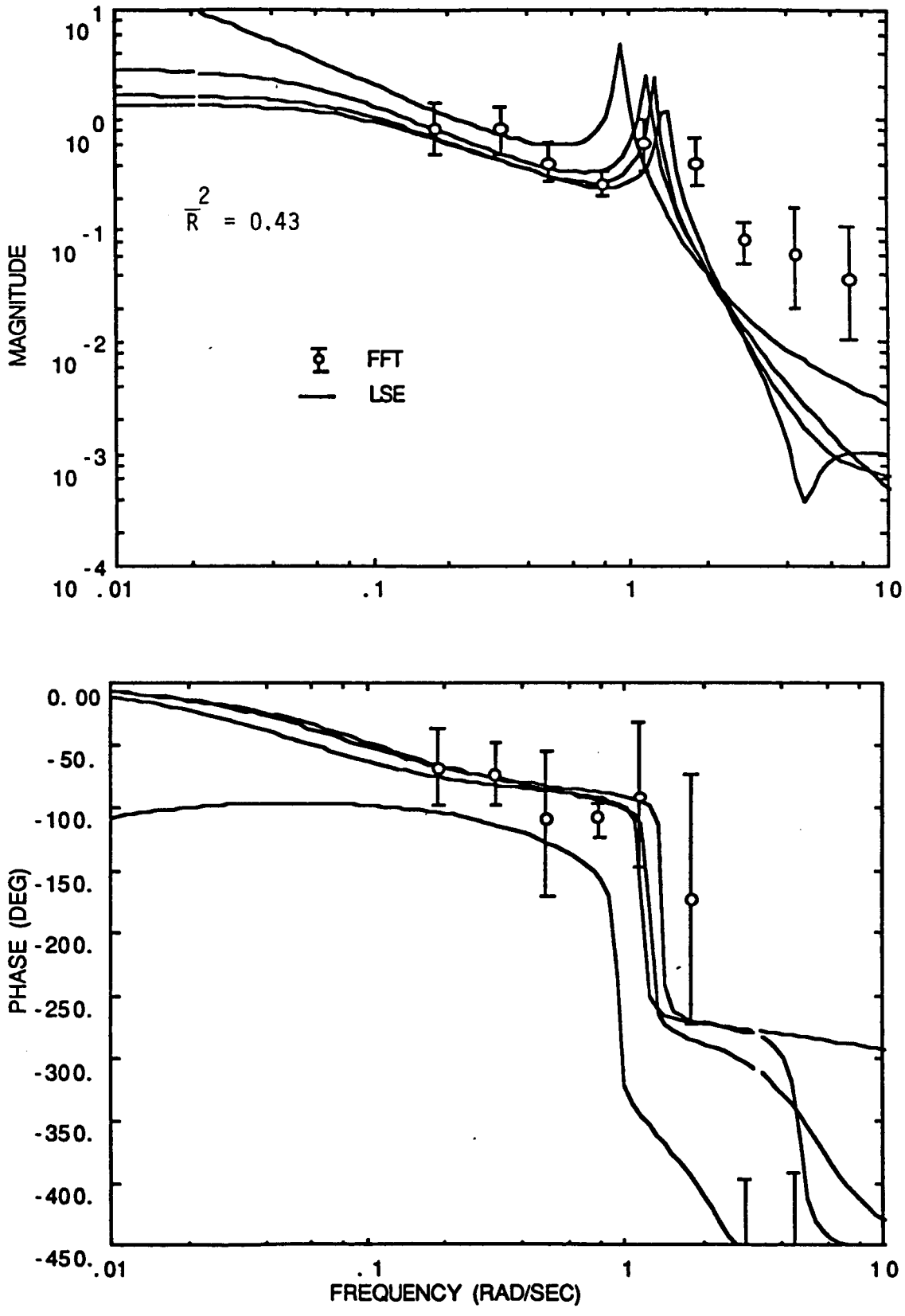
MAGNITUDE
10^{1}
10^{0}
10^{-1}
10^{-2}
10^{-3}
10^{-4}
$\bar{R}^2$ = 0.43
FFT
LSE
.01
.1
1
10
PHASE (DEG)
0. 00
-50.
-100.
-150.
-200.
-250.
-300.
-350.
-400.
-450.
FREQUENCY (RAD/SEC)

Fig. 9

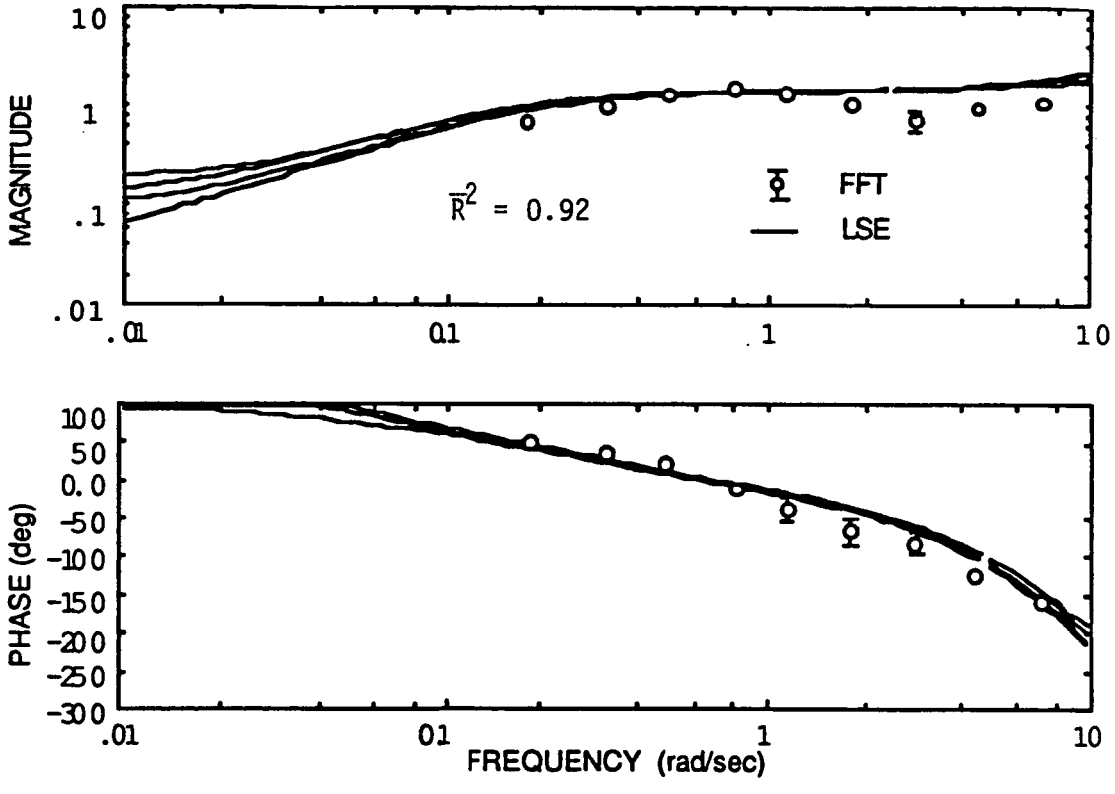
10
1
.1
.01
MAGNITUDE
$\bar{R}^2$ = 0.92
FFT
LSE
.01
.1
1
10
100
50
0.0
-50
-100
-150
-200
-250
-300
PHASE (deg)
.01
.1
1
10
FREQUENCY (rad/sec)

Fig. 10

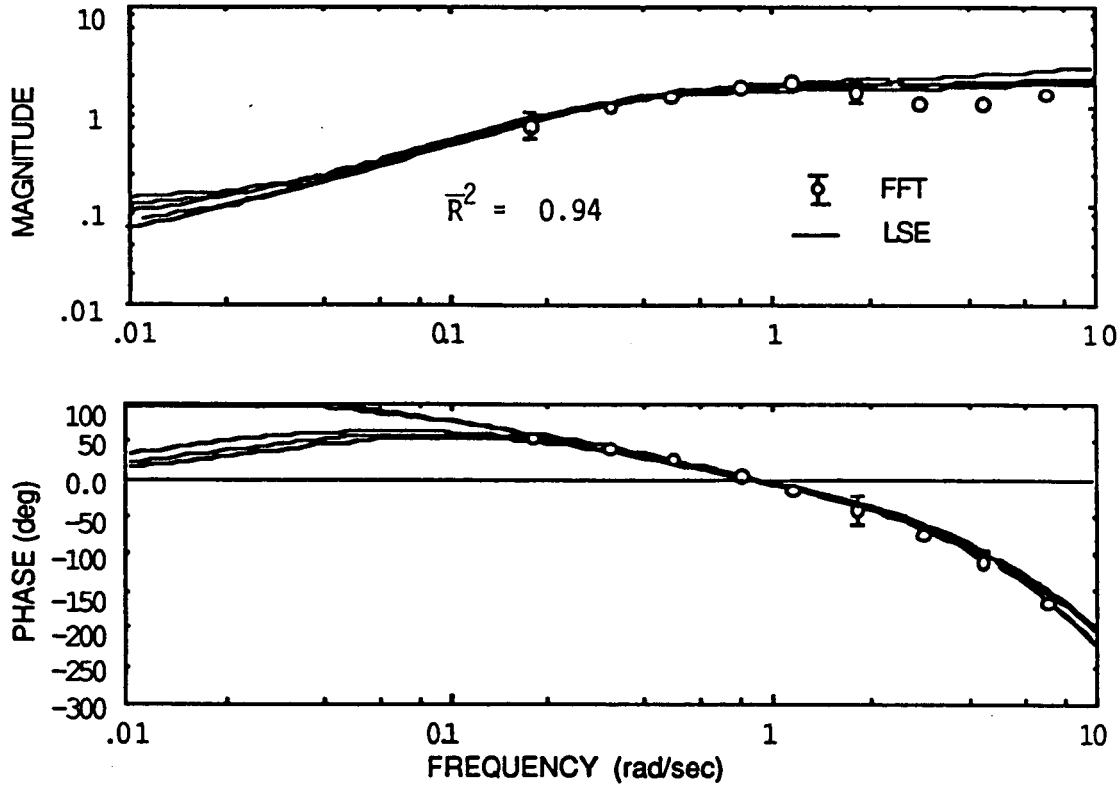
MAGNITUDE
10
1
.1
.01
$\overline{R}^2$ = 0.94
FFT
LSE
.01
0.1
1
10
PHASE (deg)
100
50
0.0
-50
-100
-150
-200
-250
-300
.01
0.1
1
10
FREQUENCY (rad/sec)

Fig. 11

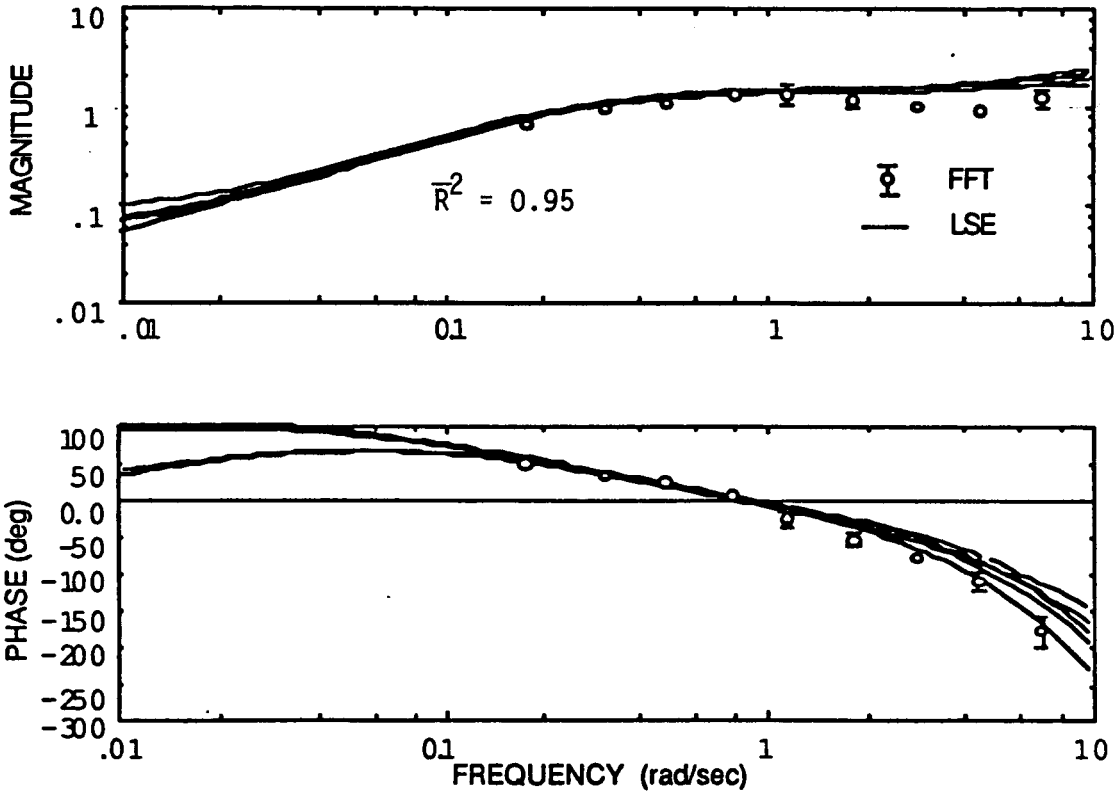
MAGNITUDE
10
1
.1
.01
.01
.1
1
10
$\bar{R}^2$ = 0.95
FFT
LSE
PHASE (deg)
100
50
0.0
-50
-100
-150
-200
-250
-300
.01
.1
1
10
FREQUENCY (rad/sec)

Fig. 12

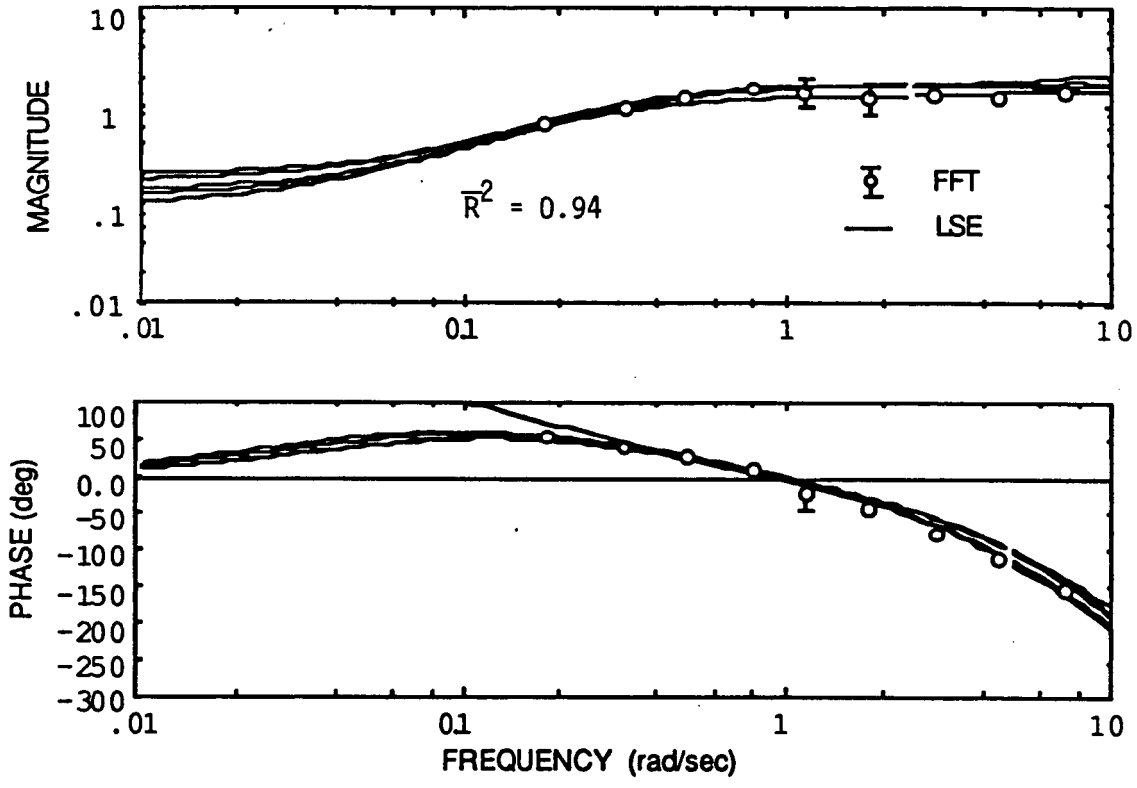
MAGNITUDE
10
1
.1
.01
.01
0.1
1
10
$\overline{R}^2$ = 0.94
FFT
LSE
PHASE (deg)
100
50
0.0
-50
-100
-150
-200
-250
-300
.01
0.1
1
10
FREQUENCY (rad/sec)

Fig. 13

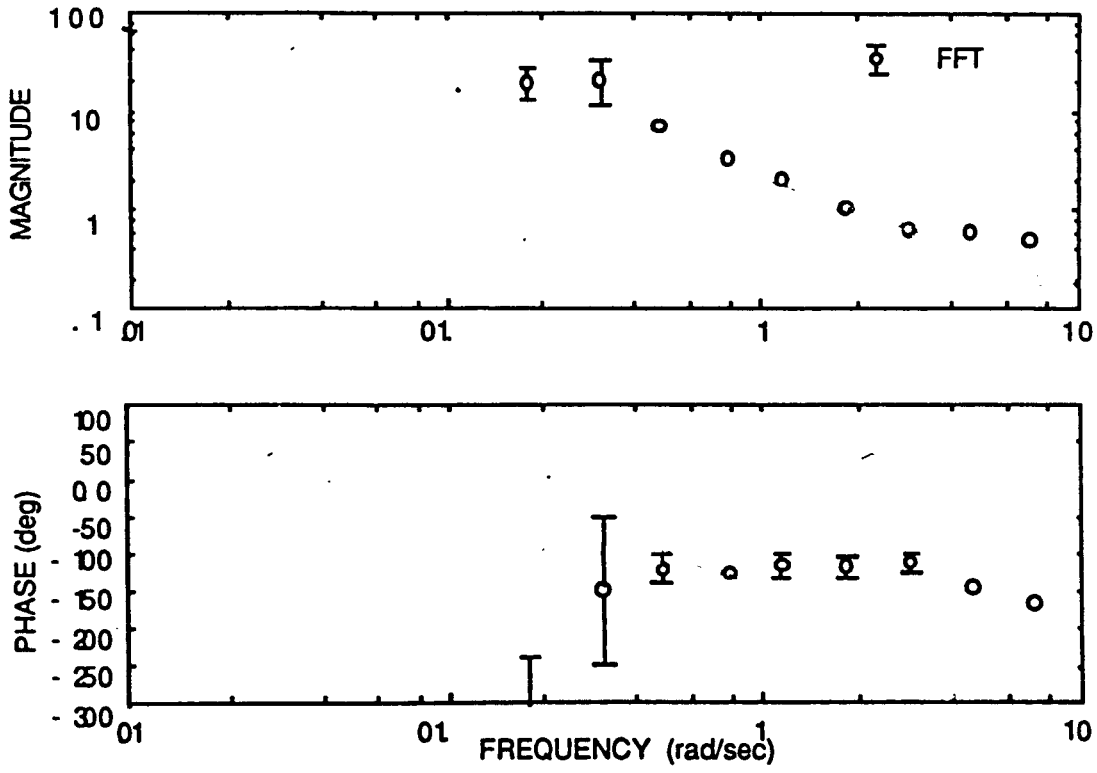
100
10
1
.1
MAGNITUDE
FFT
01
01
1
10
100
50
00
-50
-100
-150
-200
-250
-300
PHASE (deg)
01
01
1
10
FREQUENCY (rad/sec)

Fig. 14

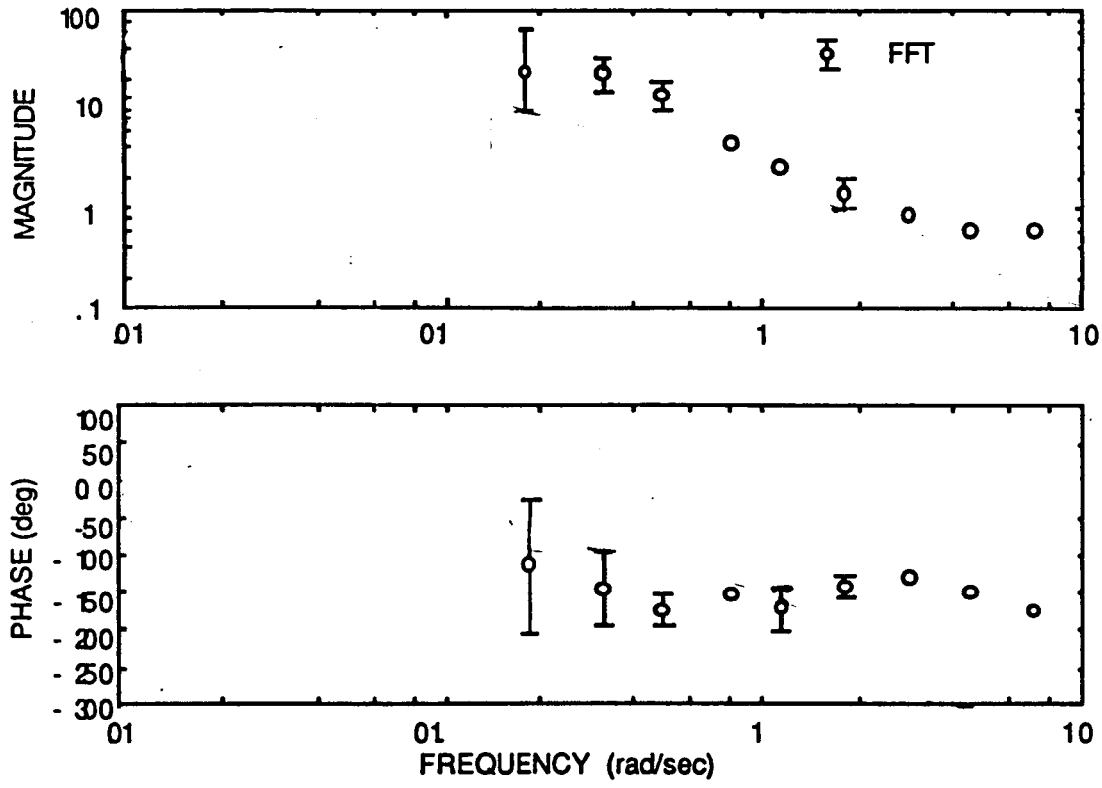
100
10
1
.1
MAGNITUDE
FFT
01
01
1
10
100
50
0 0
-50
- 100
- 150
- 200
- 250
- 300
PHASE (deg)
01
01
1
10
FREQUENCY (rad/sec)

Fig. 15

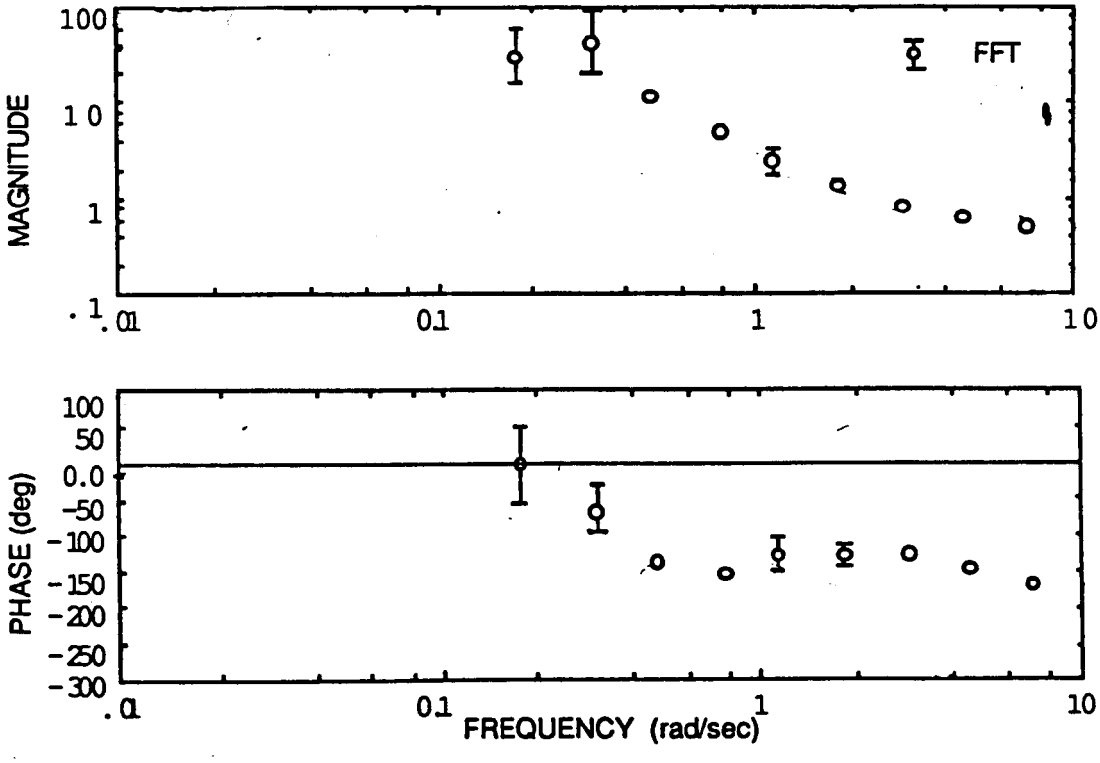
MAGNITUDE
100
10
1
.1
.01
0.1
1
10
FFT
PHASE (deg)
100
50
0.0
-50
-100
-150
-200
-250
-300
.01
0.1
1
10
FREQUENCY (rad/sec)

Fig. 16

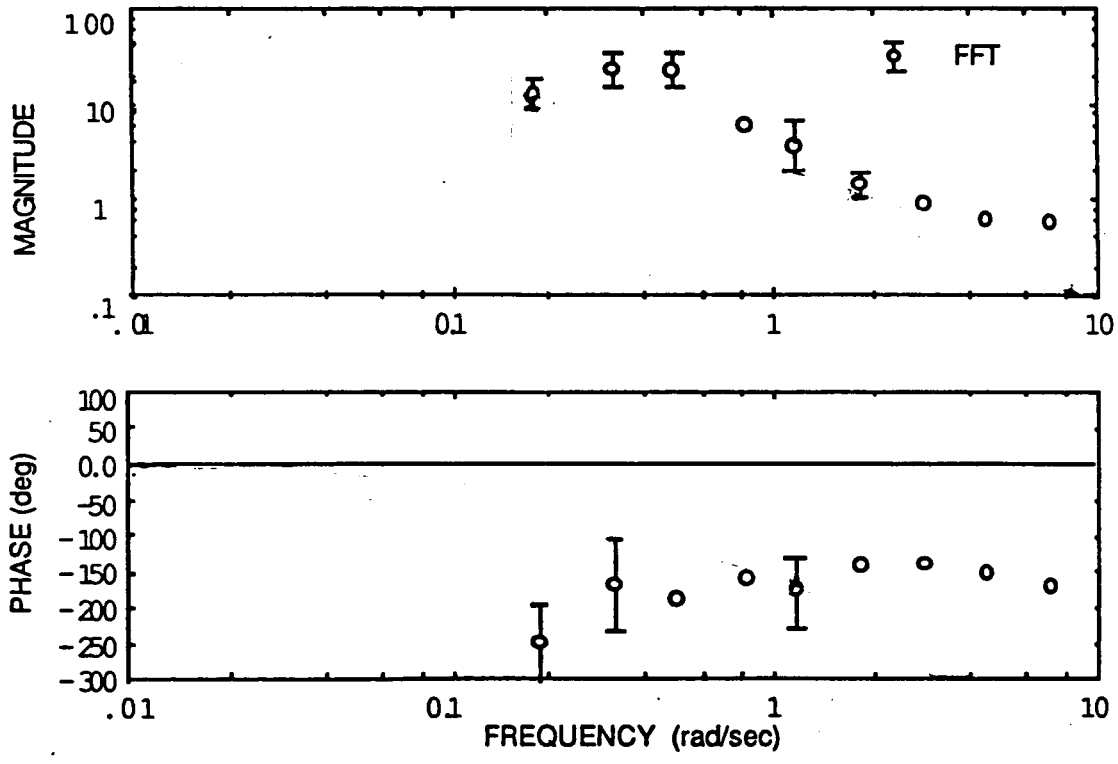
MAGNITUDE
100
10
1
.1
.01
0.1
1
10
FFT
PHASE (deg)
100
50
0.0
-50
-100
-150
-200
-250
-300
.01
0.1
1
10
FREQUENCY (rad/sec)

Fig. 17

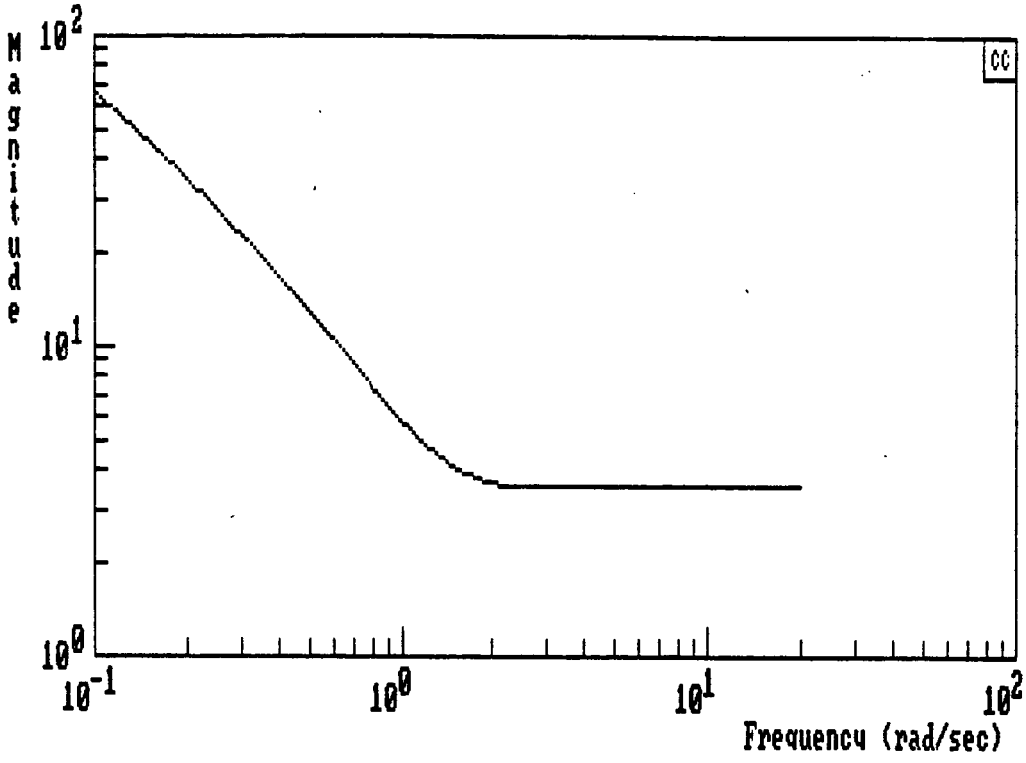
Magnitude
10^2
10^1
10^0
cc
10^{-1}
10^0
10^1
10^2
Frequency (rad/sec)

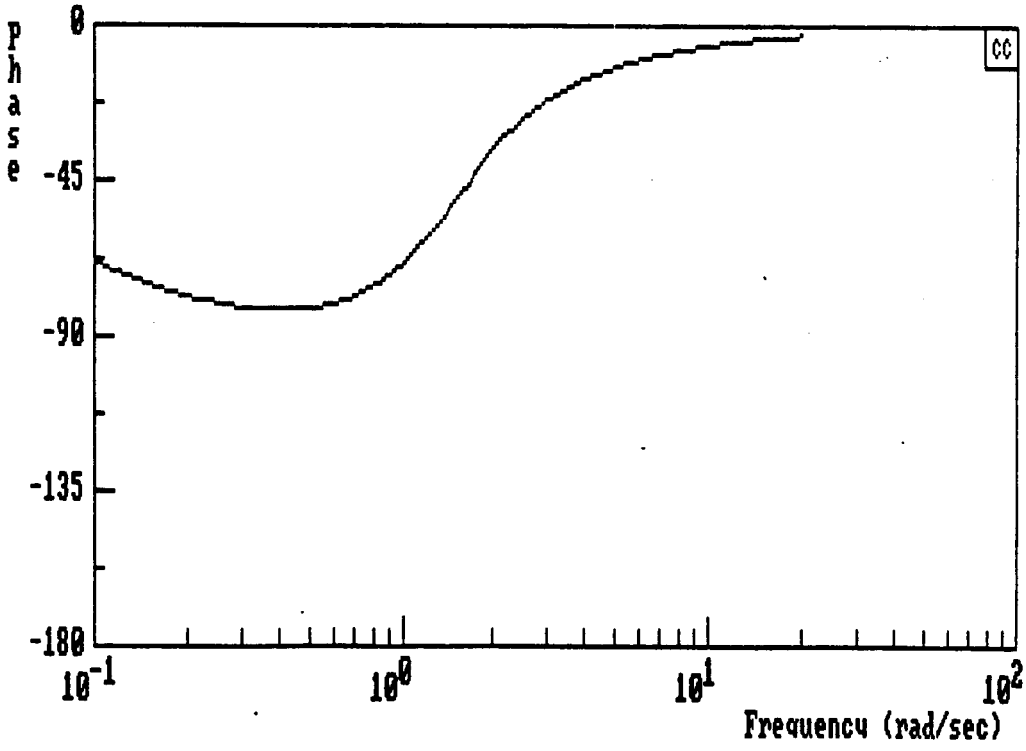
phase
0
-45
-90
-135
-180
cc
10^{-1}
10^0
10^1
10^2
Frequency (rad/sec)

Fig. 18

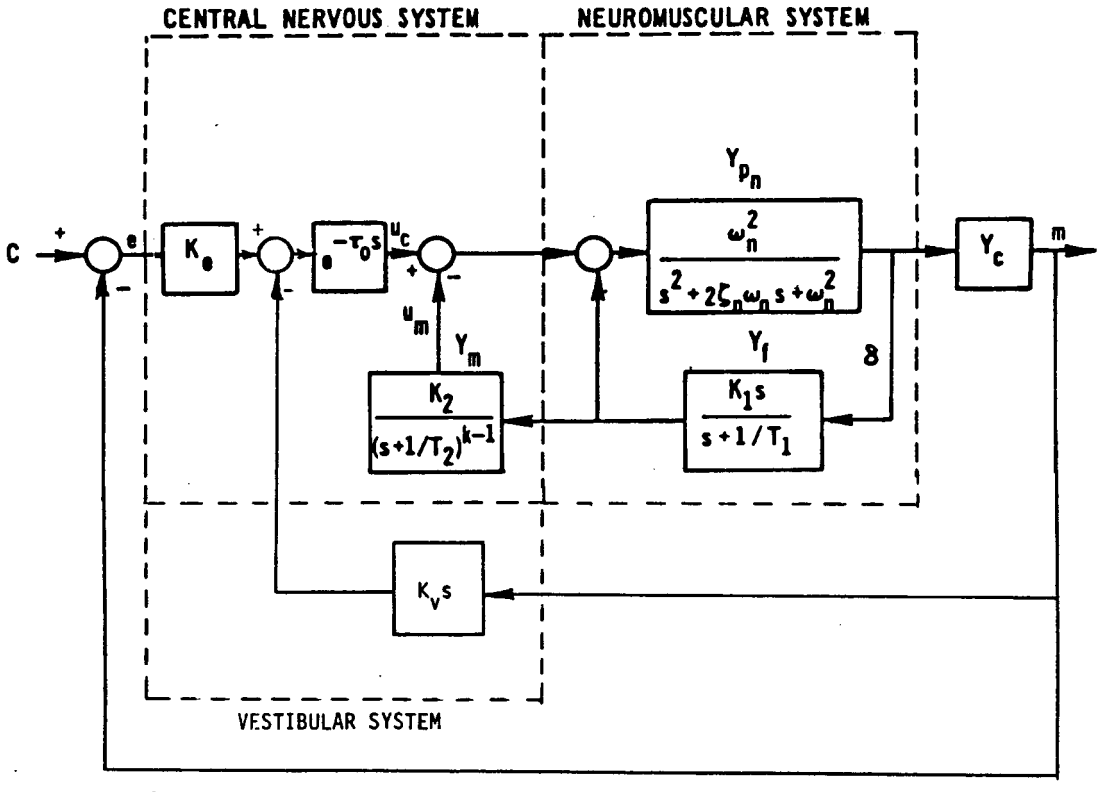
CENTRAL NERVOUS SYSTEM
NEUROMUSCULAR SYSTEM
c
e
K_e
$e^{-\tau_0 s}$
u_c
u_m
Y_m
$\frac{K_2}{(s+1/T_2)^{k-1}}$
Y_{p_n}
$\frac{\omega_n^2}{s^2+2\zeta_n\omega_n s+\omega_n^2}$
Y_c
m
Y_f
$\frac{K_1 s}{s+1/T_1}$
δ
$K_v s$
VESTIBULAR SYSTEM

Fig. 19

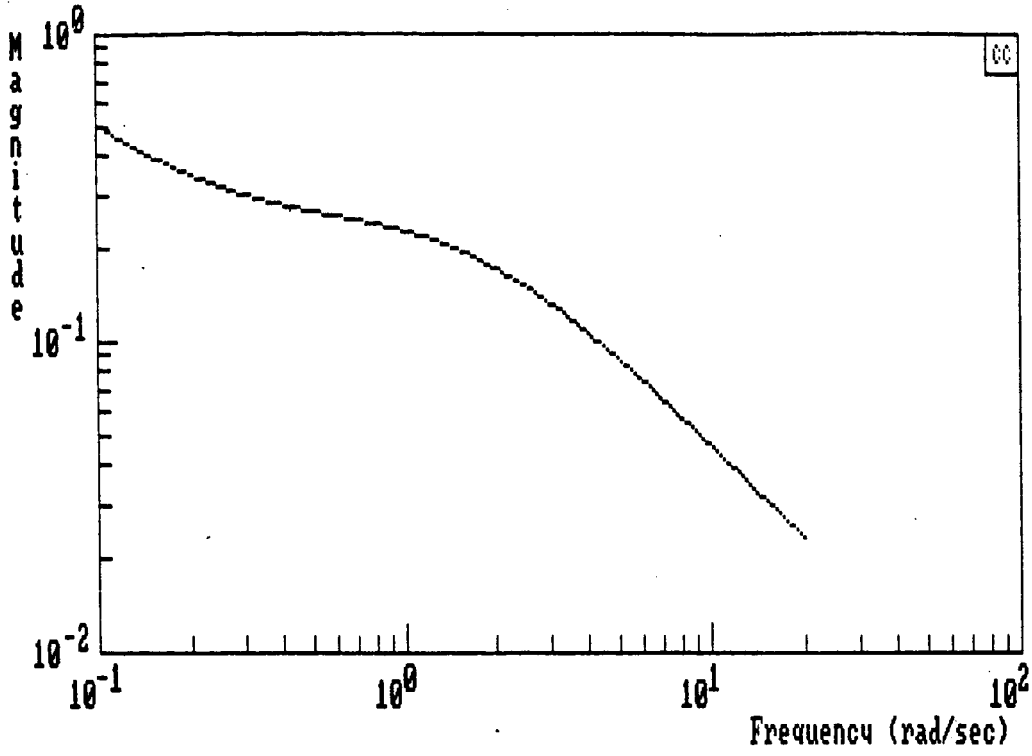
Magnitude
10^{0}
10^{-1}
10^{-2}
CC
10^{-1}
10^{0}
10^{1}
10^{2}
Frequency (rad/sec)

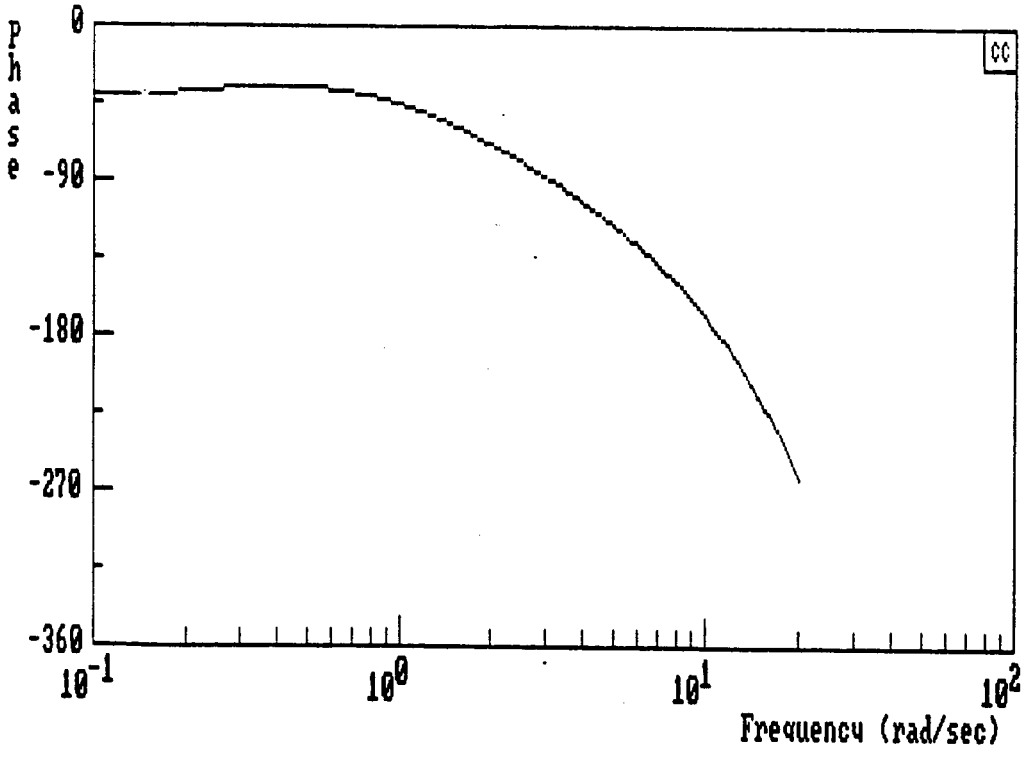
phase
0
-90
-180
-270
-360
CC
10^{-1}
10^{0}
10^{1}
10^{2}
Frequency (rad/sec)

Fig. 20

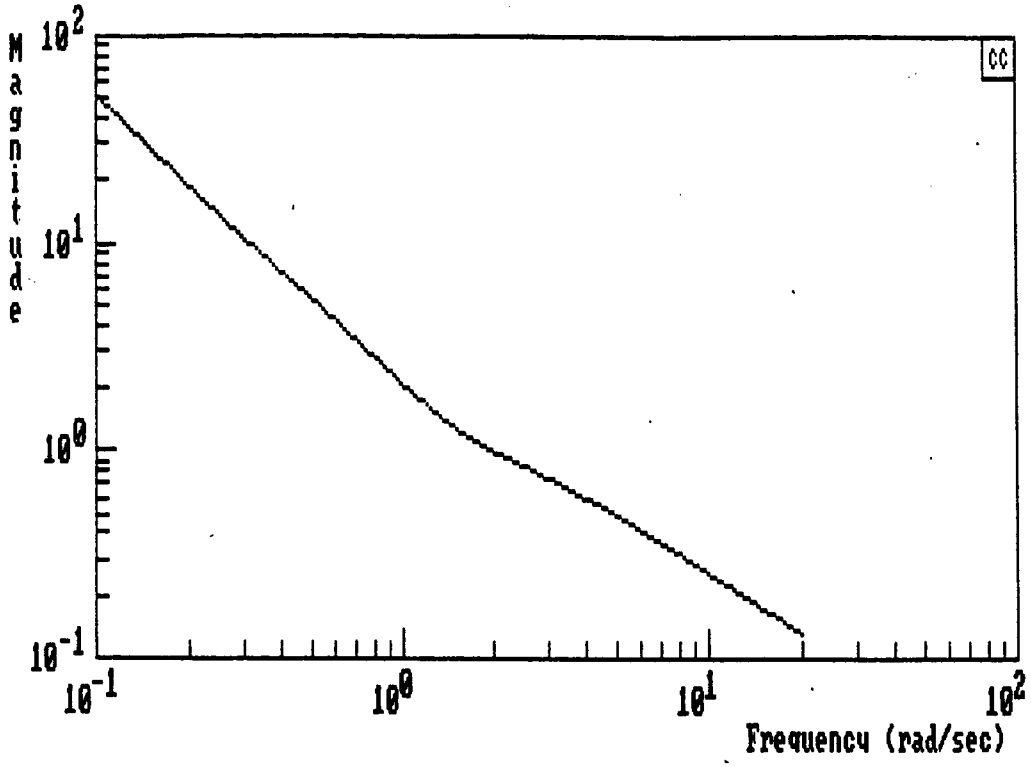
Magnitude
10^2
10^1
10^0
10^{-1}
10^{-1}
10^0
10^1
10^2
Frequency (rad/sec)
CC

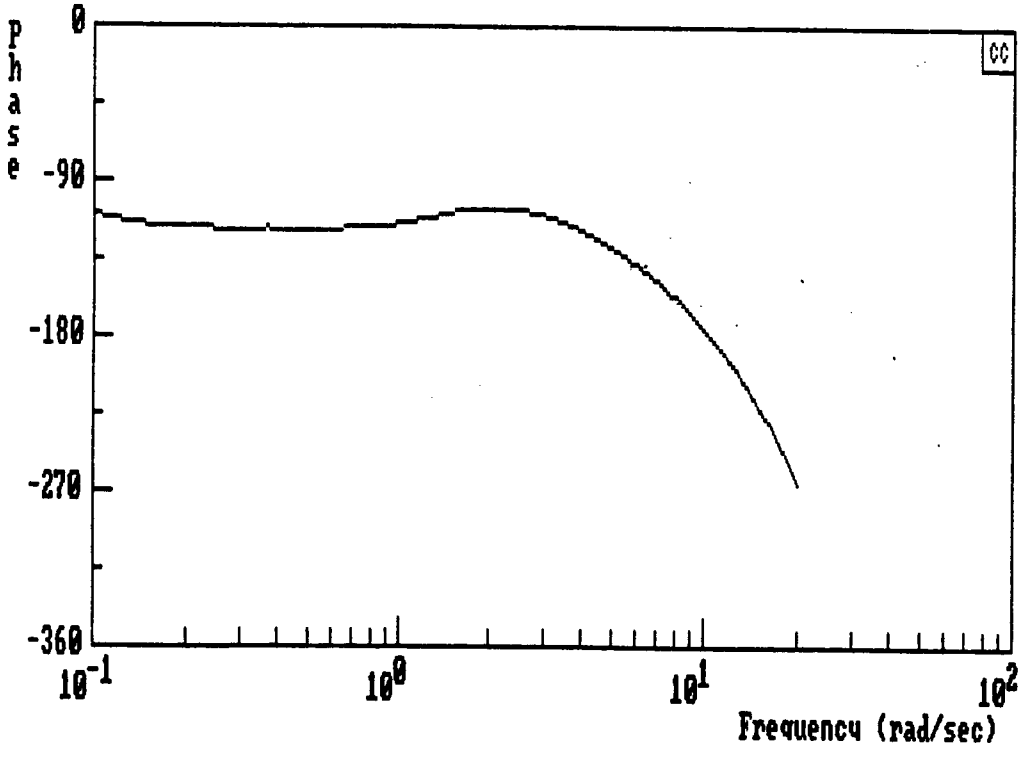
phase
0
-90
-180
-270
-360
10^{-1}
10^0
10^1
10^2
Frequency (rad/sec)
CC

Fig. 21

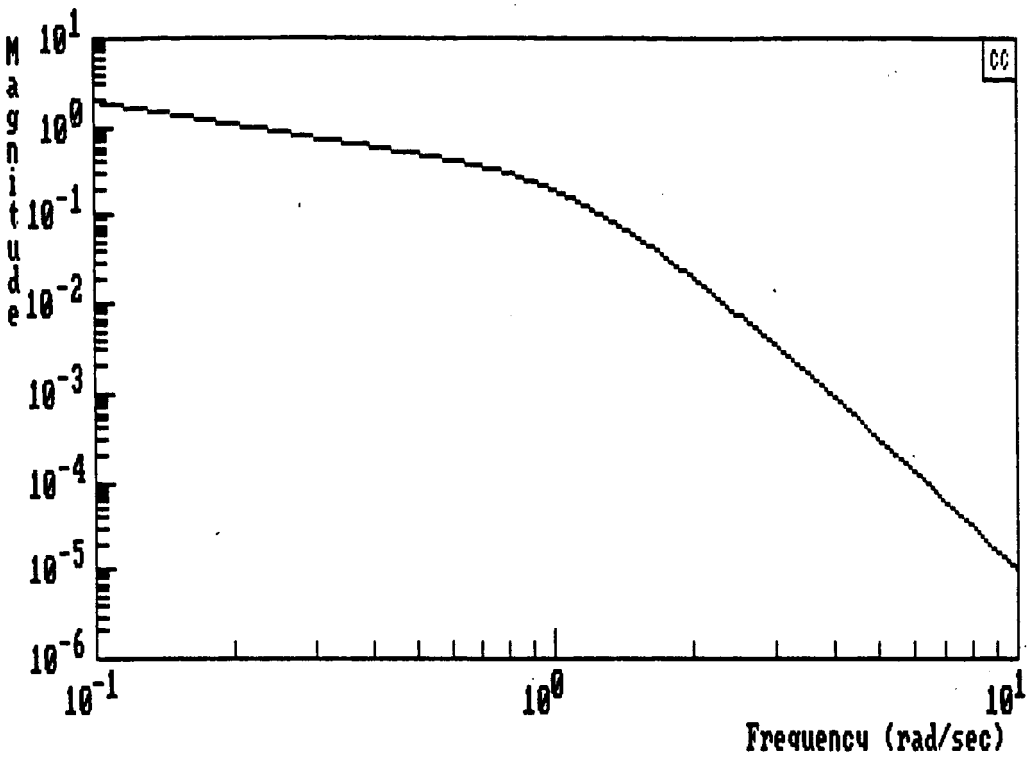
Magnitude
10^{1}
10^{0}
10^{-1}
10^{-2}
10^{-3}
10^{-4}
10^{-5}
10^{-6}
10^{-1}
10^{0}
10^{1}
Frequency (rad/sec)
CC

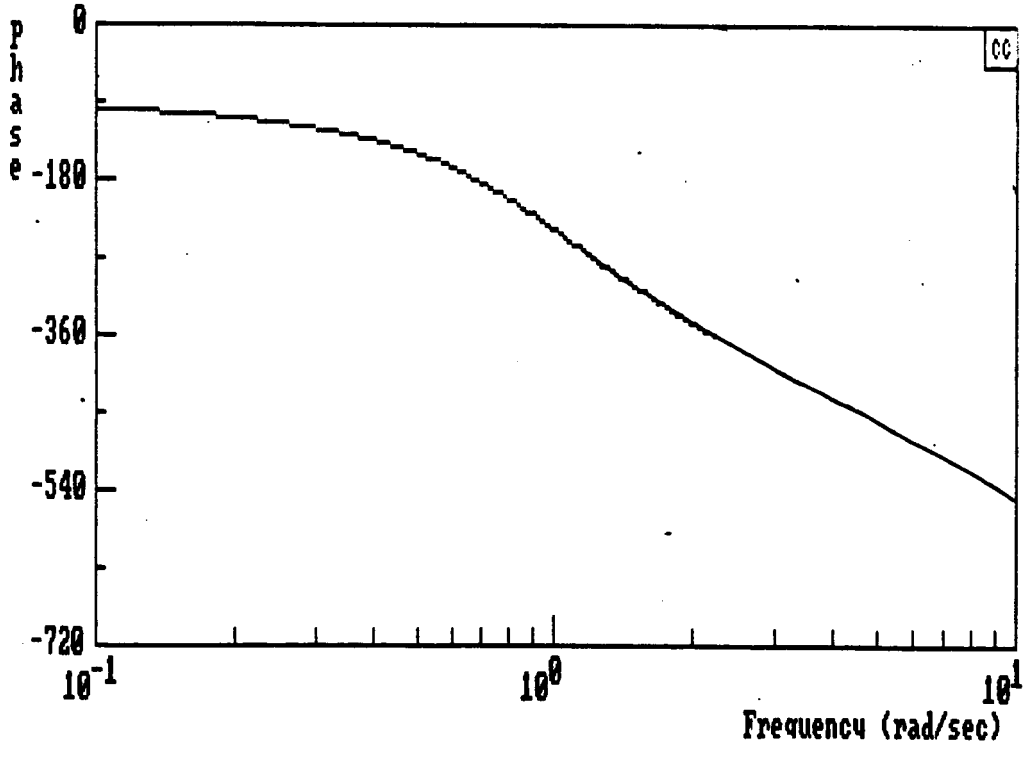
phase
0
-180
-360
-540
-720
10^{-1}
10^{0}
10^{1}
Frequency (rad/sec)
CC

Fig. 22

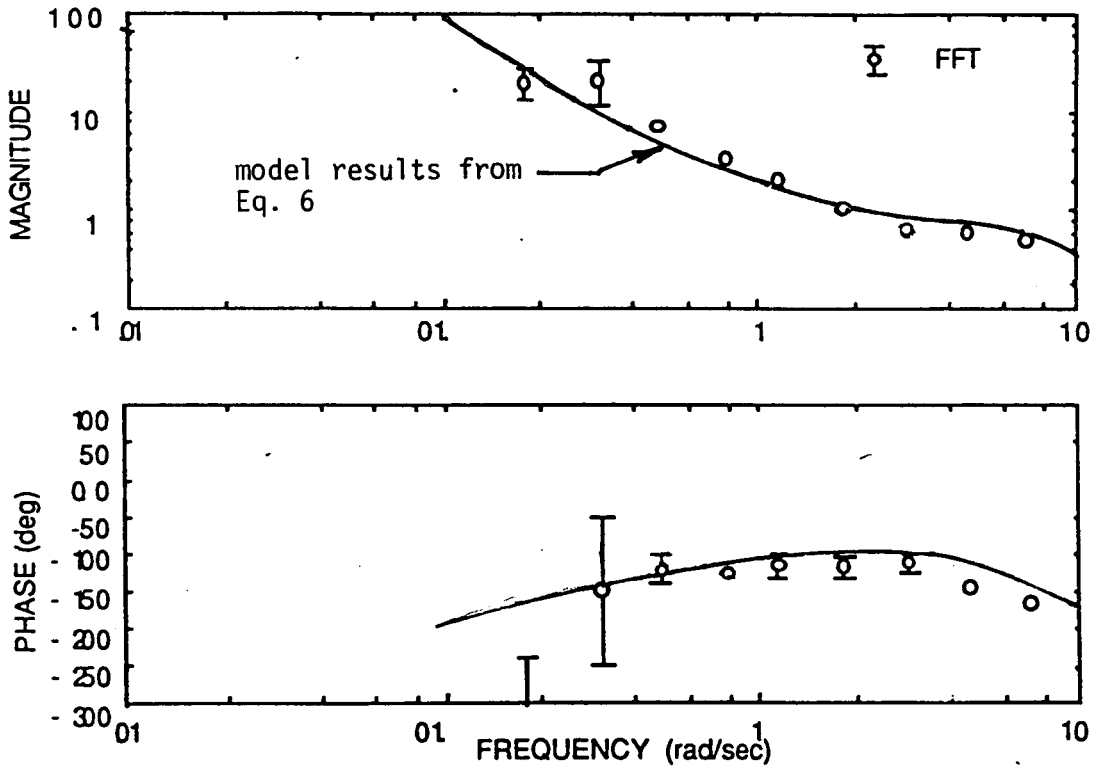
100
10
1
.1
MAGNITUDE
FFT
model results from
Eq. 6
01
01
1
10
100
50
0 0
-50
- 100
- 150
- 200
- 250
- 300
PHASE (deg)
01
01
1
10
FREQUENCY (rad/sec)

Fig. 23

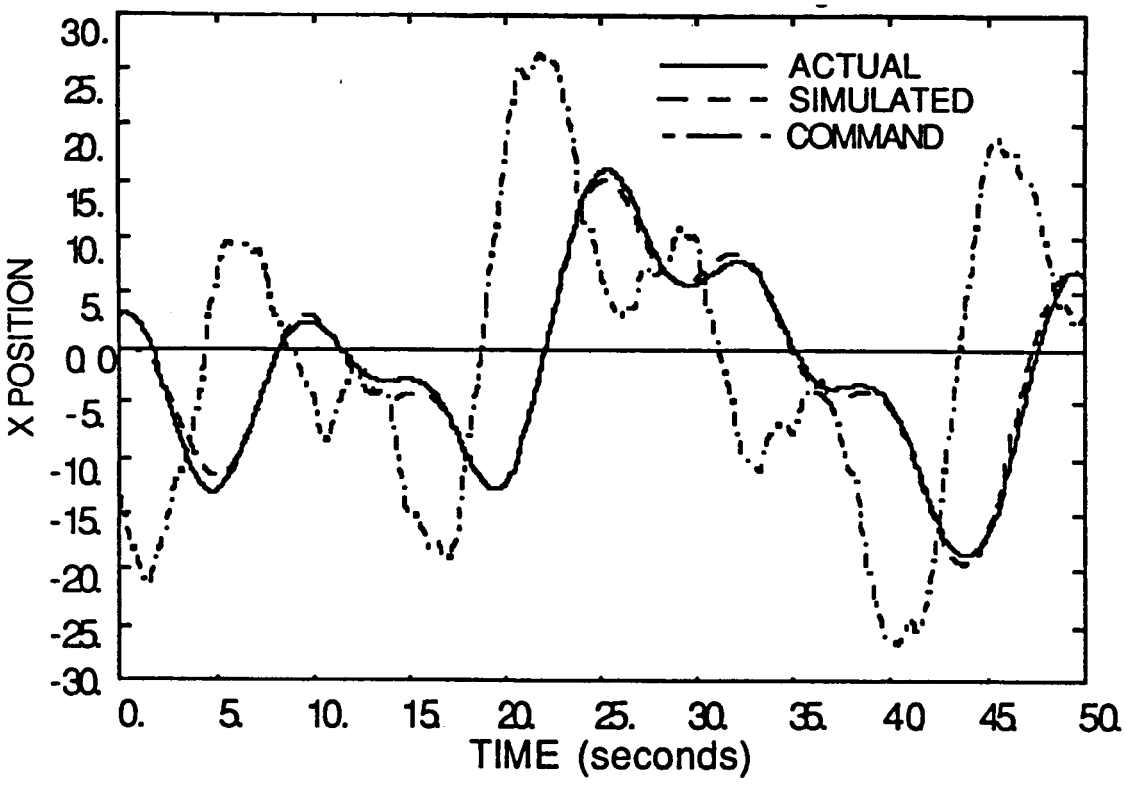
ACTUAL
SIMULATED
COMMAND
X POSITION
TIME (seconds)
30.
25.
20.
15.
10.
5.
0.0
-5.
-10.
-15.
-20.
-25.
-30.
0.
5.
10.
15.
20.
25.
30.
35.
40.
45.
50.

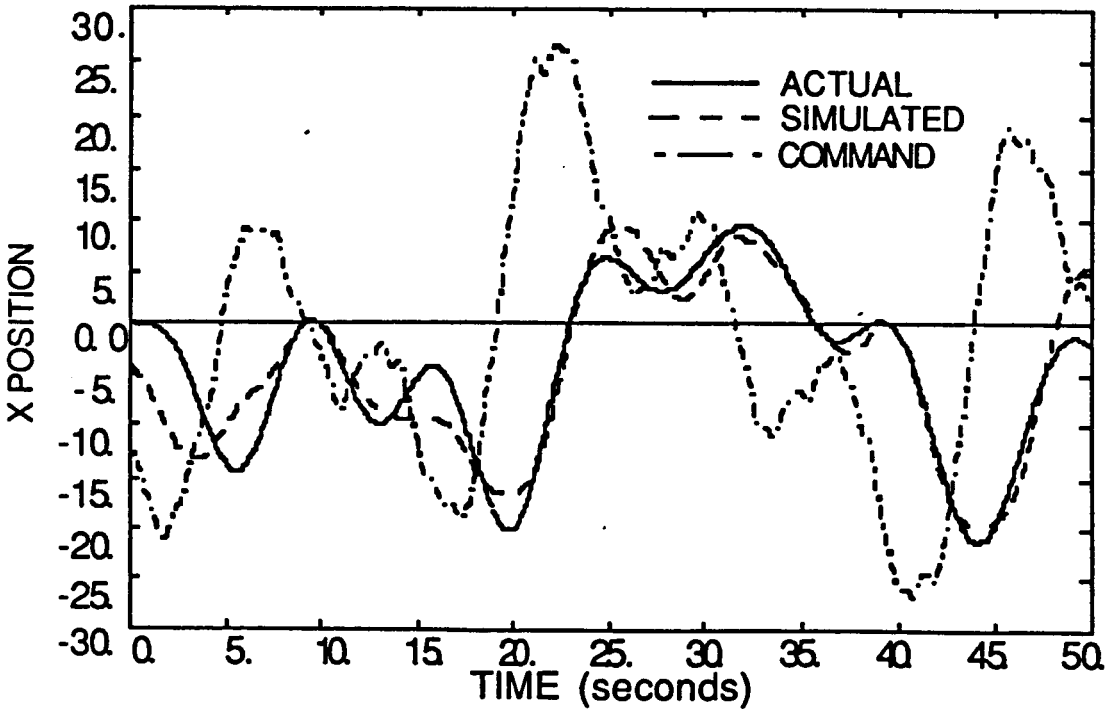
ACTUAL
SIMULATED
COMMAND
X POSITION
TIME (seconds)
30.
25.
20.
15.
10.
5.
0.0
-5.
-10.
-15.
-20.
-25.
-30.
0.
5.
10.
15.
20.
25.
30.
35.
40.
45.
50.

Fig. 24